Modelling gas fracturing in saturated clay samples using triple-node zero-thickness interface elements

Liaudat, Joaquín; Dieudonné, Anne Catherine; Vardon, Philip J.

DOI
10.1016/j.compgeo.2022.105128

Publication date
2023

Document Version
Final published version

Published in
Computers and Geotechnics

Citation (APA)
Liaudat, J., Dieudonné, A. C., & Vardon, P. J. (2023). Modelling gas fracturing in saturated clay samples using triple-node zero-thickness interface elements. *Computers and Geotechnics*, *154*, Article 105128. https://doi.org/10.1016/j.compgeo.2022.105128

Computers and Geotechnics 154 (2023) 105128

Contents lists available at ScienceDirect

Computers and Geotechnics

journal homepage: www.elsevier.com/locate/compgeo

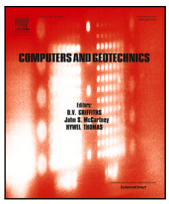

Research paper

Modelling gas fracturing in saturated clay samples using triple-node zero-thickness interface elements

Joaquín Liaudat *, Anne-Catherine Dieudonné, Philip J. Vardon

Faculty of Civil Engineering and Geosciences, Delft University of Technology, 2628 CN Delft, The Netherlands

ARTICLE INFO

Keywords:
Clay
Gas migration
Gas fracturing
Two-phase flow
Finite Element Method
Interface elements

ABSTRACT

Geological Disposal Facilities (GDF) for radioactive waste will generally rely on clay-rich materials as a host geological formation and/or engineered barrier. Gas will be produced within the GDF, which can build up significant gas pressure and will activate the migration of gas through the clay materials via different transport mechanisms. These transport mechanisms are usually investigated in laboratory tests on small clay samples of a few centimetres. In this paper, a new Pneumo-Hydro-Mechanical (PHM) Finite Element model to simulate gas migration in saturated clay samples of this scale is presented. In the proposed modelling approach, continuum elements are used to represent the mechanical and flow processes in the bulk clay material, while zero-thickness interface elements are used to represent existing or induced discontinuities (cracks). A new triple-node PHM interface element is presented to achieve this. The performance of model is illustrated with synthetic benchmark examples which show the ability of the model to reproduce observed PHM mechanisms leading to propagation of cracks due to the gas pressure (gas fracturing).

1. Introduction

High-level radioactive waste (HLW) exists throughout the world, mainly as a result of power generation. It is a long-lasting waste, characterised by low volumes but high level of radioactivity. The most likely long-term solution for HLW is the disposal in stable geological layers in the deep subsurface. Clay and claystone are considered as potential host rocks for geological disposal of HLW in several countries. Clay-based materials are also expected to be used in engineered barriers in about all repository designs under development.

Over the lifespan of a Geological Disposal Facility (GDF), a large amount of gas is expected to be produced as a result of metal corrosion, water radiolysis and bio-degradation (Ortiz et al., 2002). Due to the very low permeability of the engineered and natural clay barriers, high gas pressure may develop inside the GDF. The migration of gas under these conditions may have detrimental effects on the effectiveness of the clay barriers to prevent the transport of radionuclides to the biosphere.

As proposed by Marschall et al. (2005), four basic gas transport mechanisms in clay-based materials are distinguished based on phenomenological considerations (Fig. 1): (i) advection and diffusion of gas dissolved in the pore water, (ii) visco-capillary two-phase flow, (iii) dilatancy controlled gas flow (pathway dilation), and (iv) gas transport along macroscopic tensile fractures (gas fracturing). The activation and prevalence of each of these mechanisms depend not only on the hydraulic and mechanical properties of the clay (permeability, gas-entry value, mechanical strength, etc.), but also on the gas pressure at the injection locus and the hydro-mechanical state of the clay (i.e. pore pressure and stress state).

In Fig. 1, the four mechanisms are schematically illustrated for a Representative Elementary Volume (REV) of clay. The REV is considered to be initially fully saturated with a pore liquid phase at a pressure p_w. Dissolved gas is present in the liquid phase at a concentration characterised by an equivalent gas phase pressure p_g (smaller than p_w) through Henry's law. The material is considered to be initially under a compressive stress state determined by the total maximum and minimum principal stresses σ_1 and σ_3. Gas is produced in or injected to the REV at a constant rate and with an evolving injection pressure $\bar{p}_g$.

Upon gas injection, the first gas transport mechanism which occurs is diffusion of dissolved gas (Fig. 1, i). The process is mainly governed by Henry's law and Fick's law. If a liquid pressure gradient is developed, the dissolved gas is also transported by the advective flow of the pore water. The gas injection pressure ($\bar{p}_g$) grows until the rate at which gas is evacuated by the diffusion/advection mechanism equalises the gas injection rate, reaching at this point a steady state. As long as the injection pressure remains low, diffusion/advection is the only gas transport mechanism, the sample remains fully saturated and the effective stress field within the sample remains unaltered. However,

* Corresponding author.
E-mail addresses: J.Liaudat@tudelft.nl (J. Liaudat), A.A.M.Dieudonne@tudelft.nl (A.-C. Dieudonné), P.J.Vardon@tudelft.nl (P.J. Vardon).

https://doi.org/10.1016/j.compgeo.2022.105128
Received 30 November 2021; Received in revised form 28 October 2022; Accepted 2 November 2022
Available online 15 November 2022

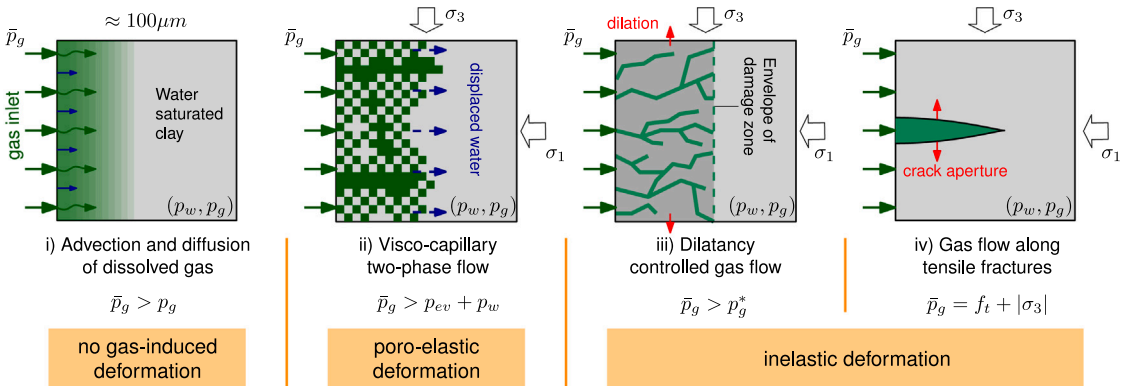

Fig. 1. Gas transport processes in water saturated clay depending on the relation between the injection pressure $\bar{p}_g$ with the state variables p_w (liquid phase pressure), p_g (gas phase pressure), and σ_3 (minimum compressive principal stress), and the material properties p_{ev} (gas-entry value) and f_t (tensile strength). Adapted from Marschall et al. (2005).

if the injection pressure grows beyond certain threshold values, other transport mechanisms will be activated.

The visco-capillary two-phase flow is characterised by the displacement of pore water in the clay by a gas phase under the strong influence of viscous and capillary forces (Fig. 1, ii). This transport process is activated as soon as the difference between the gas and the liquid phase pressures, i.e. the capillary pressure p_c, is greater than the gas-entry value p_{ev}, a material property determined by the pore structure of the clay. Once the gas-entry value is exceeded, the gas mobility is controlled mostly by the intrinsic permeability k, the retention properties, and the relative permeability function of the clay. As gas invades the clay pores, the effective pore pressure increases and, consequently, the effective compressive stress in the REV is reduced. This leads to changes in the pore structure, which in turn drives changes in the transport and retention properties. As long as these changes remain small and reversible (elastic), the transport regime is still considered to be visco-capillary two-phase flow.

In contrast, the dilatancy controlled gas flow is the mechanism whereby gas pressure induces localised consolidation and/or microfractures, such that the porosity is locally enhanced, leading to significant increase in permeability and reduction of the gas-entry value (Cuss et al., 2014) (Fig. 1, iii). Due to the micro-scale variability of the mechanical clay properties, microfractures may form before the pore pressure reaches the minimum principal stress (Marschall et al., 2005), i.e. under macroscopic compression. The gas pressure threshold for the development of this mechanism (p_g^*, in Fig. 1) has not been clearly determined yet. It is speculated that p_g^* is a function not only of the pore liquid pressure, the macroscopic stress state and the macroscopic material parameters, but also of the spatial distribution of the hydro-mechanical properties at lower scales of observation, which would in turn determine a non-uniform effective stress field in the sample. Some time-dependency of p_g^* associated to local creep or consolidation may also be expected. Moreover, visual examination of samples after gas migration tests (centimetre-scale samples) indicated that the dilatancy controlled gas flow does not develop uniformly across the sample section but concentrates on some preferential paths (Volckaert et al., 1995; Harrington et al., 2012).

Finally, gas fracturing refers to the gas-driven formation of macroscopic fractures when the gas pressure reaches the sum of the minimum principal stress (σ_3) and the material tensile strength (f_t) (Fig. 1, iv). The fractures will propagate in the plane normal to the minimum principal stress. Gas flow along these fractures can be seen mainly as a single-phase flow process controlled by the increase of the fracture transmissivity with the cube of the fracture aperture (cubic law).

For an exhaustive literature review on gas transport mechanisms in clayey materials, the reader is referred to the recent report on the state of the art of the HORIZON 2020 project EURAD, Work Package Gas (Levasseur et al., 2021).

Due to the complexity of these processes, the use of numerical models has become usual for the interpretation of experimental results. Different models have been proposed. In most cases, Finite Element Method (FEM) two-phase Hydro-Mechanical (HM) models are used (e.g. Alonso et al., 2006; Olivella and Alonso, 2008; Arnedo et al., 2008, 2013; Gerard et al., 2014; Gonzalez-Blanco et al., 2016; Damians et al., 2020; Xu et al., 2013; Guo and Fall, 2018; Dagher et al., 2019; Yang et al., 2020). In these models, the porosity, the intrinsic permeability and/or the gas-entry value are not constant but evolving with the material strain state (Alonso et al., 2006; Olivella and Alonso, 2008; Arnedo et al., 2008, 2013; Gerard et al., 2014; Gonzalez-Blanco et al., 2016; Damians et al., 2020; Xu et al., 2013; Dagher et al., 2019; Yang et al., 2020) or the gas pressure (Xu et al., 2013). The expressions governing these evolutions are proposed empirically (Dagher et al., 2019; Xu et al., 2013) or are derived from assumptions regarding the presence of discontinuities in the material matrix (Alonso et al., 2006; Olivella and Alonso, 2008; Arnedo et al., 2008, 2013; Gerard et al., 2014; Gonzalez-Blanco et al., 2016; Damians et al., 2020; Yang et al., 2020). An exception within this modelling approach is the double porosity and double effective stress model proposed by Fall and co-workers (2018, 2021a, 2021b) for modelling dilatancy controlled gas flow. This model considers the clay material as consisting of two overlapping but independent continua (the cracked continuum and the porous continuum). The interaction between the two sub-continua, resulting from the water exchange and the porosity transformation between pores and cracks, determines the permeability and the water retention properties of the material.

Simpler modelling approaches have been also proposed, such as FE purely hydraulic two-phase models (Senger et al., 2008, 2018) and Finite Volume HM single-phase (gas) models (Chittenden et al., 2020), which have shown to be able to match experimental data. In Senger et al. (2008, 2018), it is considered that the intrinsic permeability of the clay increases with the gas pressure based on empirical functions. In Chittenden et al. (2020), it is assumed that gas flow only occurs through emerging capillary tubes open by compressing the solid (clay and immobile interlayer water) when gas pressure exceeds a threshold stress, which depends on the total stress of the system. Under these assumptions, expressions of the gas permeability and porosity as functions of the gas pressure and the total stress are obtained. By reducing the number of degrees of freedom of the problem, the computational cost of these models is significantly smaller than that of the coupled HM two-phase models. However, this is done at the expense of reducing the applicability of these models to situations where the assumptions regarding the neglected degrees of freedoms are valid.

It is noteworthy that only the models where material heterogeneity is explicitly accounted for Delahaye and Alonso (2002), Alonso et al. (2006), Arnedo et al. (2008, 2013), Senger et al. (2018) and Damians et al. (2020) were able to reproduce the formation of preferential

gas flow pathways. In the remaining models, the alteration of the solid skeleton by the gas pressure and the consequent variation of permeability and gas-entry value does not lead to a localisation of the advective gas flow.

Although the possibility of tensile cracks due to the gas pressure is considered in some of the previous models, this is done in an implicit way. In the Embedded Fracture Models (Alonso et al., 2006; Olivella and Alonso, 2008; Arnedo et al., 2008, 2013; Gerard et al., 2014; Gonzalez-Blanco et al., 2016; Damians et al., 2020), tensile strains are converted into equivalent crack apertures by assuming a crack density (number of cracks per unit length) which is given as a material parameter. The gas flow along the cracks is not explicitly represented but implicitly considered by increasing the intrinsic permeability and decreasing gas-entry value of the integration where the tensile strains are developed. To the best of the authors' knowledge, the only model that explicitly considers the propagation of gas fractures in clay-based materials is the Phase Field (PF) model proposed by Guo and Fall (2019). Parting from a typical FEM two-phase HM model, an additional scalar auxiliary variable called PF is used to regularise the sharp discontinuity produced by tensile cracks as diffuse crack zones. Cracked zones receive the same treatment as the intact zones (two-phase flow porous medium) but with distinct material parameters. A regularisation parameter l determines the width of the transition between intact and cracked zones. The smaller the l parameter, the better the representation of the crack. Moreover, a reasonable accuracy of the crack topology approximation requires FE meshes with element size smaller than $l/2$ (Miehe et al., 2010). Due to these restrictions, the model requires very fine FE meshes for a good representation of cracks.

Of the previously referred models, only Alonso et al. (2006), Olivella and Alonso (2008), Arnedo et al. (2008, 2013), Gerard et al. (2014), Gonzalez-Blanco et al. (2016), Damians et al. (2020) and Dagher et al. (2019) consider the diffusion–advection of dissolved gas in the pore water simultaneously with the other gas transport mechanisms. The other models neglect the contribution of the diffusion–advection of dissolved gas to the overall gas migration process.

In this paper, a numerical model is outlined which aims at simulating gas injection tests in small samples of few centimetres in order to aid the interpretation of experimental results. The model has the distinctive characteristic of explicitly representing the gas fracturing mechanism via a discrete fracture approach, in combination with advection–diffusion of dissolved gas and visco-capillary two-phase flow in the bulk clay material.

In the following section, the main aspects and the background of the proposed modelling approach are described. Sections 3 to 5 summarise the formulation of the model. The model performance is illustrated with benchmark examples in Section 6. Concluding remarks on the model achievements of the model are provided in the final section.

2. Modelling approach

The gas migration in water saturated clay is modelled in 2D and isothermal conditions using a Pneumo-Hydro-Mechanical (PHM) formulation discretised with FEM. In the proposed modelling approach, continuum elements are used to represent the mechanical and flow processes in the bulk clay material, while zero-thickness interface elements are used to represent existing or induced discontinuities (cracks). The interface elements are introduced a priori in between the continuum elements, thereby providing a set of potential propagation paths for cracks (Fig. 2). The constitutive laws of the interface elements are such that, as long as they remain closed, they do not have any significant effect on the overall hydro-mechanical response of the modelled clay sample. However, when a certain mechanical threshold is reached (e.g. the tensile strength) and the interface element starts to open, localised mechanical and flow processes are triggered. Similar approaches can be found in the literature for modelling hydraulic fracturing of rocks (Carrier and Granet, 2012; Nguyen et al., 2017; Rueda-Cordero et al., 2019b,a) and concrete cracking due to chemo-mechanical processes (Idiart et al., 2011a,b; Liaudat et al., 2020). In addition, interface elements can be used to represent interfaces between different materials (e.g. the contact between a clay sample and steel cells used in lab tests) or existing discontinuities (e.g. bedding planes).

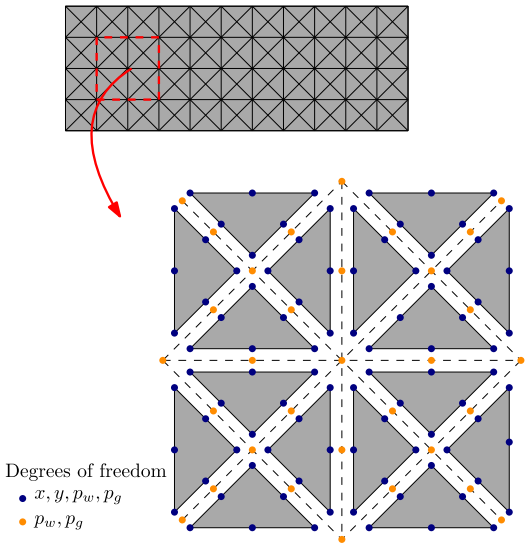

Fig. 2. Introduction of zero-thickness interface elements in a conventional FE mesh. Adapted from Rueda-Cordero et al. (2019a).

This approach has the conceptual advantage of treating the continuum and discontinuities as two separate (though connected) subdomains within the clay material. In that way, different (though consistent) mechanical and flow constitutive laws can be used for the continuum porous medium and for the induced cracks or pre-existent discontinuities, allowing a more realistic representation of the effect of discontinuities in the clay material.

As a negative counterpart, cracks can only develop at the pre-established lines where the interface elements have been inserted. This is a discretisation of a continuum problem. In reality, the potential cracking paths for a given boundary value problem are infinite, such that the propagation of cracks will form the pattern that requires exactly the minimum mechanical work. In contrast, with the proposed modelling approach the cracking pattern will be the one that requires the least mechanical work among the set of potential patterns provided by the adopted FE mesh with interface elements. This pattern is not necessarily the one requiring the minimum minimorum mechanical work for the boundary value problem considered, but it will be the closest among the available options. In that way, the refinement of the FE mesh makes it possible to more closely approximate the actual cracking pattern, and, therefore, the proposed modelling approach is mesh convergent. Nonetheless, previous studies of cracking processes with this approach, though considering cement-based materials, suggested that the macroscopic response is not significantly influenced by the precise location of the cracks as long as the initial layout of interfaces is 'reasonable', i.e. it includes all major potential cracking paths without excessive tortuosity (López, 1999; Carol et al., 2001; López et al., 2008). In any case, a post-process analysis of the evolution of the stress state in the continuum elements and a mesh sensitivity analysis must be always conducted to assess the suitability of the proposed mesh and propose a new discretisation, if needed.

The interface elements adopted for this model are of the triple-node type (Fig. 2). The top and bottom face nodes, which are shared with the adjacent continuum elements, have four degrees of freedom (x, y coordinates, liquid phase pressure p_w, and gas phase pressure p_g), while inner nodes have only two (p_w and p_g). (Interface elements of the double-node type are those which only have nodes on the top

and bottom faces.) The insertion of these elements in conventional FE meshes is performed with a separate programme which has been developed adapting the algorithm proposed by Nguyen (2014).

The flow problem is treated in the typical theoretical framework for isothermal two-phase flow in porous medium, considering two chemical species (water and gas) and two fluid phases (liquid and gas phases). The liquid phase includes both liquid water and dissolved gas species, while the gas phase only comprises gas species, i.e. water vapour is not considered.

The mechanical problem is treated with an updated Lagrangian formulation, i.e. geometric non-linearity is taken into account. Finite strain theory is considered for the continuum elements, though small tangential relative displacements are assumed for the discontinuities. In the latter, a node-to-node discretisation of the contact area is used. In a first approach, simple constitutive laws are considered for both types of elements. The continuum medium is assumed to behave linear-elastically, while a simple bilinear elasto-damage law is used for the discontinuities, which is formulated in terms of relative displacements rather than strains. Note that the use of a cohesive-type constitutive relation to represent fracture leads to an automatic regularisation from the viewpoint of objectivity of the mechanical (fracture) problem with mesh refinement (Carol et al., 2001), which is a significant advantage of the proposed modelling approach. In establishing the equilibrium equation, quasi-static conditions are assumed, i.e. dynamic forces are neglected. Since the model will be mainly used to simulate injection tests in samples of a few centimetres, body (gravity) forces are neglected.

The coupling between the mechanical and the flow formulations occurs in both directions. On one hand, the fluid phase pressures and the saturation degree are introduced in the mechanical equilibrium equation through the principle of effective stress. On the other hand, the flow properties (gas-entry value, storage capacity, longitudinal transmissivity and diffusivity) vary dramatically, governed largely by the mechanical aperture of the discontinuity. To deal with these strong couplings, a monolithic (fully coupled) numerical implementation is used.

The continuum medium part of the model follows the formulation proposed by Collin et al. (2002) and Gerard et al. (2008), without introducing significant changes. In contrast, for modelling the discontinuities a new triple-node PHM interface element has been developed using a node-to-node discretisation of the contact problem. The new interface element borrows concepts from previous works by Segura and Carol (2004, 2008b,a), who developed a double-node HM interface element with node-to-node contact discretisation, and by Cerfontaine et al. (2015) and Dieudonné et al. (2015), who developed a triple-node PHM interface element with segment-to-segment contact discretisation. Although the new interface element is presented in 2D, the formulation developed is valid and readily extensible to 3D.

In the segment-to-segment contact discretisation, the zones at each side of the discontinuity that are going to interact with each other are not defined a priori and may change during the simulation. For that reason, elements with segment-to-segment contact discretisation are able to model large relative displacements properly, although at the expense of a high computational cost. In contrast, in the node-to-node contact discretisation, the interacting zones at each side are defined a priori and are assumed to remain the same during the simulation. This assumption leads to a much lower computational cost, although restricting the applicability of this kind of element to problems with small tangential relative displacements. A brief review on contact discretisation methods can be found in Cerfontaine et al. (2015).

Note that the systematic use of interface elements all over the mesh, as illustrated in Fig. 2, has the disadvantage of significantly increasing the number of degrees of freedom in comparison with standard continuum analysis. For the 2D analyses presented in this paper this increase of the computational cost can be afford, but 3D analysis would require a remedy. For instance, Pandolfi and Ortiz (1998) proposed a procedure based on calculation of inter-element forces to duplicate nodes and insert interface elements as needed.

3. PHM governing equations for the continuum porous medium

3.1. Mechanical problem

After neglecting the body forces, the linear momentum balance equation of the continuum porous medium reads as follows:

$$\nabla \cdot \boldsymbol{\sigma} = \mathbf{0} \tag{1}$$

where $\boldsymbol{\sigma}$ [Pa] is the Cauchy's total stress tensor. The sign convention of continuum mechanics (i.e. tensile stress is positive) is used in this paper.

The constitutive behaviour of the continuum porous medium is formulated in terms of the effective stress tensor $\boldsymbol{\sigma}'$ and its conjugate strain tensor $\boldsymbol{\varepsilon}$. The material is assumed isotropic and linear elastic, with parameters E [Pa] (Young's modulus) and ν (Poisson's coefficient). The effective stress results from considering the effect of the pore fluid pressures acting on the solid grains of the porous medium via the following expressions:

$$\boldsymbol{\sigma}' = \boldsymbol{\sigma} + b p_s \mathbf{I} \tag{2}$$

$$p_s = S_w p_w + S_g p_g \tag{3}$$

where b is the Biot's coefficient, $\mathbf{I}$ is the identity tensor, and p_s [Pa] is the effective pore pressure, and p_π [Pa] and S_π [m^3/m^3] are the pressure and pore saturation degree of the fluid phase π ($\pi = w$ for the liquid phase and $\pi = g$ for the gas phase), respectively. The liquid saturation degree is obtained as a function solely of the capillary pressure ($p_c = p_g - p_w$), as it is described later in Section 3.2.4. Since the pore space is assumed to be fully saturated with the liquid and gas phases, $S_g = 1 - S_w$.

3.2. Flow problem

3.2.1. Mass balance

The mass balance equations of gas and water species in a REV of porous medium are given by:

$$\frac{\partial}{\partial t}\left(n S_w \rho_{\mathrm{w}w}\right) + \nabla \cdot \mathbf{q}_{\mathrm{w}} = 0 \tag{4}$$

$$\frac{\partial}{\partial t}\left(n S_w \rho_{\mathrm{g}w} + n S_g \rho_{\mathrm{g}g}\right) + \nabla \cdot \mathbf{q}_{\mathrm{g}} = 0 \tag{5}$$

where n is the porosity, $\rho_{\varsigma\pi}$ [kg/m^3] is the mass concentration of ς species in the fluid phase π, and $\mathbf{q}_\varsigma$ [$kg/(m^2\ s)$] is the average mass flow vector of the ς species. Note that w and g subindexes (in Italic type) are used to denote the liquid and gas phases, while w and g subindexes (in Roman type) are used to denote water and gas species. The storage terms in Eqs. (4) and (5) couple the mechanical and the flow formulations via the porosity rate, which is obtained with the following expression:

$$\frac{\partial n}{\partial t} = (n - b)\left(C_s \frac{\partial p_s}{\partial t} + \frac{\partial \varepsilon_v}{\partial t}\right) \tag{6}$$

where C_s [1/Pa] is the compressibility (the inverse of the bulk modulus) of the solid grains, and $\varepsilon_v = \mathrm{tr}(\boldsymbol{\varepsilon})$ is the volumetric strain of the porous medium.

3.2.2. Equations of state

Only one species is considered in the gas phase, so the density of the gas phase and the density of gas species in the gas phase are the same, i.e. $\rho_{\mathrm{g}g} = \rho_g$. Then, assuming ideal gas behaviour, the density of the gas phase is obtained as follows:

$$\rho_g = \frac{M_{\mathrm{g}}}{RT} p_g \tag{7}$$

where M_{g} [kg/mol] is the molar weight of the gas species, $R = 8.314$ [$(m^3\ Pa)/(K\ mol)$] is the gas constant, T [K] is the system temperature.

The mass of gas species dissolved per a unit volume of liquid phase (ρ_{gw} [kg/m^3]) is obtained, assuming local equilibrium, with the following Henry's law equation:

$$\rho_{gw} = H\rho_g \tag{8}$$

where H is the dimensionless Henry solubility constant for the gas species in liquid water. It is assumed that the dissolved gas has a negligible effect on the density of the liquid phase, and therefore, it is considered that $\rho_{ww} = \rho_w$.

The liquid phase density is assumed to depend linearly on the liquid phase pressure according to the following expression:

$$\rho_w = \rho_{w,o}\left[1 + C_w\left(p_w - p_{w,o}\right)\right] \tag{9}$$

where $\rho_{w,o}$ [kg/m^3] and C_w [1/Pa] are the water density and compressibility, respectively, at the reference pressure $p_{w,o}$.

3.2.3. Mass flows

The mass flow vectors in Eqs. (4) and (5) can be expanded as follows:

$$\mathbf{q}_w = \rho_{ww}\mathbf{v}_w \tag{10}$$

$$\mathbf{q}_g = \rho_{gw}\mathbf{v}_w + \rho_{gg}\mathbf{v}_g + \mathbf{i}_{gw} \tag{11}$$

where $\mathbf{v}_\pi$ [m/s] is the average (Darcy) velocity of the fluid phase π, and $\mathbf{i}_{gw}$ [kg/(m^2 s)] is the average diffusive flow of gas species dissolved in the pore water.

The average fluid phase velocities are obtained with the following two-phase generalisation of Darcy's law:

$$\mathbf{v}_\pi = -\frac{k_{\pi,r}}{\mu_\pi}\mathbf{k}\nabla p_\pi \quad \text{for } \pi = w, g \tag{12}$$

where $\mathbf{k}$ [m^2] is the intrinsic permeability tensor of the porous medium, μ_π [Pa s] is the dynamic viscosity of the fluid phase π, and $k_{\pi,r}$ is the dimensionless relative permeability coefficient, which ranges between 0 and 1 as a function solely of S_π.

The average diffusive flow vector of gas species in the pore water is obtained with following generalisation of Fick's law for an unsaturated porous medium:

$$\mathbf{i}_{gw} = -nS_w\tau D_{gw}\rho_w\nabla\left(\frac{\rho_{gw}}{\rho_w}\right) \tag{13}$$

where D_{gw} [m^2/s] is the diffusion coefficient of the gas species in bulk water, and τ is a dimensionless coefficient accounting for the effect of the tortuosity of the pore space.

3.2.4. Liquid retention and relative permeability

The retention behaviour of the continuum porous medium has been chosen, for simplicity, to be represented with the standard van Genuchten's model (van Genuchten, 1980):

$$S_w(p_c) = \left(1 - S_{wr}\right)\left[1 + \left(\frac{p_c}{p_b}\right)^{\frac{1}{1-\lambda}}\right]^{-\lambda} + S_{wr} \tag{14}$$

where S_{wr} is the residual degree of saturation, p_b [Pa] is a parameter related to the gas-entry value, and λ is a parameter that controls the shape of the curve.

The relative permeability coefficients for the liquid and gas phases are considered to be functions of the effective degree of saturation (S_e) according to the following power laws:

$$k_{w,r} = S_e^{n_w}; \quad k_{g,r} = (1 - S_e)^{n_g} \tag{15}$$

where n_w and n_g are dimensionless material parameters and

$$S_e = \frac{S_w - S_{wr}}{1 - S_{wr}} \tag{16}$$

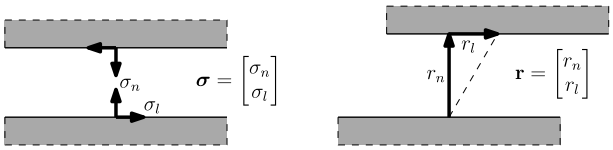

Fig. 3. Definition of stress and conjugate relative displacement variables for a discontinuity.

4. PHM governing equations for the discontinuities

4.1. Mechanical problem

The equilibrium condition for a discontinuity is given by:

$$\frac{\partial\boldsymbol{\sigma}}{\partial l} = \mathbf{0} \tag{17}$$

where $\boldsymbol{\sigma} = \begin{bmatrix}\sigma_n & \sigma_l\end{bmatrix}^\mathsf{T}$ is the total stress on the discontinuity mid-plane, with components normal (σ_n) and tangential (σ_l) to the discontinuity mid-plane (Fig. 3).

The constitutive behaviour is formulated in terms of the effective stress $\boldsymbol{\sigma}' = \begin{bmatrix}\sigma'_n & \sigma_l\end{bmatrix}^\mathsf{T}$ and the conjugate relative displacement $\mathbf{r} = \begin{bmatrix}r_n & r_l\end{bmatrix}^\mathsf{T}$ (Fig. 3). The effective stress is defined as follows:

$$\boldsymbol{\sigma}' = \boldsymbol{\sigma} + \mathbf{m}p_s \tag{18}$$

where p_s [Pa] is the effective fluid pressure at the discontinuity mid-plane, and $\mathbf{m} = \begin{bmatrix}1 & 0\end{bmatrix}^\mathsf{T}$.

The effective fluid pressure is obtained as a function of the saturation degree and the fluid phase pressures with the same expression as for the continuum porous medium (Eq. (3)). However, here the liquid saturation degree is obtained not only as a function of the capillary pressure, but also of the normal separation (r_n), as it is discussed below in Section 4.2.4. As for the continuum medium, the discontinuity is assumed to be fully saturated with the liquid and gas phases, i.e. $S_g = 1 - S_w$.

In principle, the solid domains at both sides of the discontinuity cannot overlap each other, i.e. the normal relative displacement (r_n) cannot be negative. This strict condition, which would be very demanding for the numerical resolution of the problem, is relaxed by authorising a small interpenetration of the solids in contact using the penalty method. The interpenetration is limited in the constitutive law (Section 4.1.1) by assigning a very high normal stiffness for $r_n < 0$.

4.1.1. Constitutive law

The mechanical constitutive behaviour of the discontinuity is modelled using the elasto-damage law proposed by Mi et al. (1998), combined with a Newtonian damper for the normal direction. The response of the elasto-damage law for pure normal (Mode I) and pure shear (Mode II) loading is schematically depicted in Fig. 4. Three parameters characterise each of these constitutive curves: the maximum tensile/shear strength (σ_{n0}, σ_{l0}), the normal/tangential 'cracking' separation (r_{n0}, r_{l0}) and the normal/tangential debonding separation (r_{nc}, r_{lc}). The dashed lines in Fig. 4a and b indicate the unloading–reloading path after reaching relative displacements r_n^* and r_l^*, respectively.

In the general (mixed mode) loading condition, normal and tangential stresses are obtained with the following expressions:

$$\sigma'_{n,d} = \begin{cases}(1 - D)K_n r_n & \text{if } r_n \geq 0 \\ K_n r_n & \text{if } r_n < 0\end{cases} \tag{19}$$

$$\sigma_l = (1 - D)K_l r_l \tag{20}$$

where $K_n = \sigma_{n0}/r_{n0}$ and $K_l = \sigma_{l0}/r_{l0}$ are the initial (very high) normal and tangential stiffness, respectively. In the context of this paper, these coefficients should be interpreted as penalty coefficients that must be set to values as high as possible without causing numerical problems,

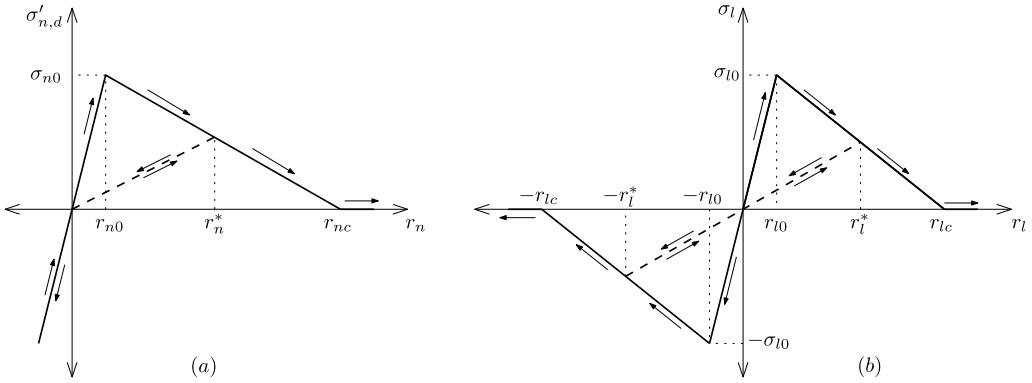

Fig. 4. Constitutive relationships for (a) pure normal loading and (b) pure tangential loading.

in order to reduce the artificial compliance introduced by the interface elements to negligible values.

Eqs. (19) and (20) are coupled through the damage variable D. The damage variable, which ranges between 0 and 1, accounts for the material softening when the normal and/or the tangential separation goes beyond the cracking separation, and it is obtained from the following expressions:

$$D = \min\left(\frac{\bar{\omega}}{1+\bar{\omega}}\frac{1}{\eta}, 1\right) \tag{21}$$

$$\bar{\omega} = \max(\omega) \tag{22}$$

$$\omega = \left\langle \left[\left(\frac{\langle r_n \rangle}{r_{n0}}\right)^{\beta} + \left(\frac{|r_l|}{r_{l0}}\right)^{\beta} \right]^{1/\beta} - 1 \right\rangle \tag{23}$$

$$\eta = 1 - \frac{r_{n0}}{r_{nc}} = 1 - \frac{r_{l0}}{r_{lc}} \tag{24}$$

where ω is a positive scalar that accounts for the mechanical degradation of the discontinuity for a given combination of normal and tangential separations, β is a material parameter that characterises the mixed mode damage and which will generally assume values between 1 and 2 (in this paper $\beta = 1$), $\bar{\omega}$ is a history variable that stores the maximum value reached by ω in the loading history, and $\langle \bullet \rangle = (\bullet + |\bullet|)/2$ is the Macaulay bracket. The restriction to the material parameter ratios r_{n0}/r_{nc} and r_{l0}/r_{lc} established in Eq. (24) guarantees that the tensile and shear strength are exhausted simultaneously (Alfano and Crisfield, 2001).

Note in Eq. (19) that, under compression loading, the constitutive response is always determined by the (very high) initial stiffness K_n, regardless the damage state of the discontinuity. In that way, the possible overlapping of the solid domains at both sides of the discontinuity under compressive loads is kept small (i.e. the penalty method). Moreover, according to Eq. (23), no damage is induced by negative normal separations.

Finally, the effective stress in the normal direction is obtained by adding a viscous component as follows:

$$\sigma'_n = \sigma'_{n,d} + \sigma'_{n,v} \text{ with } \sigma'_{n,v} = \zeta \frac{\partial r_n}{\partial t} \tag{25}$$

where ζ [Pa s/m] is the viscosity. The viscous term is included to address numerical instabilities that may develop under certain conditions and which are discussed below in Section 6.1.2.

4.2. Flow problem

The formulation of the flow problem is derived by considering a discontinuity of width w [m] surrounded by the continuum porous medium, and a local orthogonal coordinate system defined by the directions tangent ($\mathbf{e}_l$) and normal ($\mathbf{e}_n$) to the discontinuity (Fig. 5). Flow of the water and gas species may occur both in the longitudinal and in the transversal directions to the discontinuity. For the sake of simplicity, it is assumed that the longitudinal flows depend on the gas and liquid phase pressures at the centre (mid-plane) of the discontinuity width w. Consistently, the remaining parameters/variables of the discontinuity are also computed at the mid-plane, but assumed to be valid across the discontinuity width.

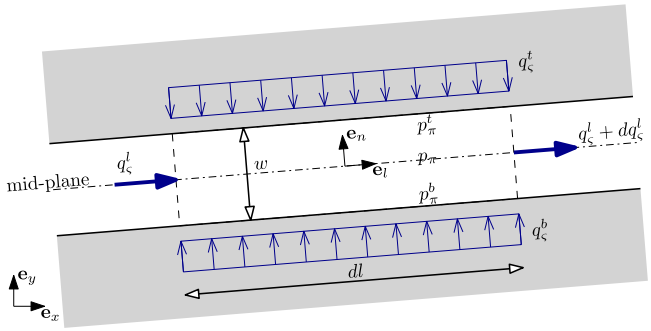

Fig. 5. Flow problem definition for a 2D discontinuity, for fluid phases $\pi = w, g$ and chemical species $\varsigma = \mathrm{w}, \mathrm{g}$.

4.2.1. Mass balance

The mass balance of gas and water species is enforced in a differential volume of discontinuity $w\mathrm{d}l$ as follows:

$$\frac{\partial}{\partial t}\left(wS_w\rho_{\mathrm{w}w}\right) + \frac{\partial q_{\mathrm{w}}^l}{\partial l} - q_{\mathrm{w}}^b - q_{\mathrm{w}}^t = 0 \tag{26}$$

$$\frac{\partial}{\partial t}\left(wS_g\rho_{\mathrm{g}g} + wS_w\rho_{\mathrm{g}w}\right) + \frac{\partial q_{\mathrm{g}}^l}{\partial l} - q_{\mathrm{g}}^b - q_{\mathrm{g}}^t = 0 \tag{27}$$

where q_ς^l [kg/(m s)] is the longitudinal mass flow of species ς, and q_ς^b and q_ς^t [kg/(m^2 s)] are the normal mass flows incoming to the discontinuity from the surrounding continuum medium. The densities $\rho_{\varsigma\pi}$ [kg/m^3] are evaluated using the same equations of state as for the continuum medium (Section 3.2.2). The liquid saturation degree is obtained as a function of the capillary pressure and the normal aperture (r_n), as it is described below in Section 4.2.4. Note that in Eqs. (26) and (27) the change of the storage capacity due to the possible change of the discontinuity length has been neglected.

The discontinuity width will evolve with r_n as follows:

$$w = \langle r_n \rangle + w_0 \tag{28}$$

where w_0 [m] makes it possible to assign an initial storage volume to the discontinuity even if it is mechanically closed.

The mass flows of gas species may be expanded as follows:

$$\begin{aligned} q_{\mathrm{g}}^l &= \rho_g v_g^l + \rho_{\mathrm{g}w} v_w^l + i_{\mathrm{g}w}^l \\ q_{\mathrm{g}}^b &= \rho_g v_g^b + \rho_{\mathrm{g}w} v_w^b + i_{\mathrm{g}w}^b \end{aligned} \tag{29}$$

$$q_g^t = \rho_g v_g^t + \rho_{gw} v_w^t + i_{gw}^t$$

where v_π^l [m²/s], v_π^t [m/s] and v_π^b [m/s] are the longitudinal and transversal volumetric flows (top and bottom) of phase π, and i_{gw}^l [kg/(m s)], i_{gw}^b [kg/(m² s)] and i_{gw}^t [kg/(m² s)] are the longitudinal and normal diffusion fluxes of gas species dissolved in the liquid phase.

Similarly, the mass flows of water species are expanded as follows:

$$q_w^l = \rho_w v_w^l; \quad q_w^b = \rho_w v_w^b; \quad q_w^t = \rho_w v_w^t \tag{30}$$

4.2.2. Volumetric fluid phase flows

The longitudinal volumetric fluid phase flows in Eqs. (29) and (30) are obtained from the following generalised Darcy's law:

$$v_\pi^l = -\frac{k_{\pi,r}}{\mu_\pi} t^l \frac{\partial p_\pi}{\partial l} \tag{31}$$

where $k_{\pi,r}$ and μ_π [Pa s] are the relative permeability and the dynamic viscosity of the fluid phase π, respectively, and t^l [m³] is the longitudinal hydraulic coefficient.

Similarly, the transversal volumetric flows are assumed to be proportional to the transversal pressure drops $\check{p}_\pi^b$ and $\check{p}_\pi^t$ between the discontinuity boundaries and the mid-plane, namely:

$$v_\pi^b = -\frac{k_{\pi,r}}{\mu_\pi} k^b \check{p}_\pi^b \quad \text{for } \pi = w, g \tag{32}$$

$$v_\pi^t = -\frac{k_{\pi,r}}{\mu_\pi} k^t \check{p}_\pi^t \quad \text{for } \pi = w, g \tag{33}$$

where k^b and k^t [m] are the transversal hydraulic coefficients. The transversal pressure drops are defined as follows:

$$\check{p}_\pi^b = p_\pi - p_\pi^b; \quad \check{p}_\pi^t = p_\pi - p_\pi^t \tag{34}$$

where p_π^b, p_π, and p_π^t [Pa] are the fluid phase pressures at the bottom side, mid-plane and top side of the discontinuity, respectively. With this definition, the transversal flows obtained with Eqs. (32) and (33) are positive when they go into the discontinuity, regardless of whether they enter through the top or the bottom face.

The hydraulic coefficients t^l, k^b and k^t are considered to be determined by the geometric characteristics of the discontinuity. In this sense, they play the role of the intrinsic permeability in the formulation for the continuum porous medium. The longitudinal coefficient is estimated as a function of the discontinuity normal aperture with the following expression:

$$t^l = \frac{\langle r_n \rangle^3}{12} + t_0^l \tag{35}$$

where the first term is given by the Hagen–Poiseuille equation for laminar flow between two parallel plates, and t_0^l makes it possible to assign an initial longitudinal transmissivity to the discontinuity even if it is closed from the mechanical point of view. In contrast, the transversal coefficients k^b and k^t are deemed constant parameters.

4.2.3. Diffusion of gas in the liquid phase

The longitudinal diffusive flow of gas species dissolved in the liquid phase, i_{gw}^l [kg/(m s)], is obtained with the following generalised Fick's law:

$$i_{gw}^l = -S_w D_{gw} d^l \rho_w \frac{\partial}{\partial l}\left(\frac{\rho_{gw}}{\rho_w}\right) \tag{36}$$

where D_{gw} [m²/s] is the diffusion coefficient of the gas species in bulk water, and d_l [m] is a coefficient that accounts for the effect of the discontinuity geometry on the diffusive flux (analogous to the product of porosity and tortuosity in the continuum medium formulation). The coefficient d^l is obtained as a linear function of the normal aperture as follows:

$$d^l = \langle r_n \rangle + d_0^l \tag{37}$$

where d_0^l makes it possible to assign an initial longitudinal diffusivity to the discontinuity even if it is closed from the mechanical point of view. This expression is based on the assumption that diffusion occurs along a clean channel of width $\langle r_n \rangle$ configured by the two faces of the discontinuity.

Considering Henry's law (Eq. (8)) and expanding the derivative, Eq. (36) can be rewritten in terms of the longitudinal gradients of gas and liquid pressures as follows:

$$i_{gw}^l = -S_w d^l D_{gw}\left(H \frac{\partial \rho_g}{\partial p_g}\frac{\partial p_g}{\partial l} - \frac{\rho_{gw}}{\rho_w}\frac{\partial \rho_w}{\partial p_w}\frac{\partial p_w}{\partial l}\right) \tag{38}$$

In addition to the longitudinal diffusive flux, normal fluxes i_{gw}^b and i_{gw}^t [kg/(m² s)] from the bottom and top sides of the discontinuity, respectively, are considered. These fluxes are obtained as follows:

$$i_{gw}^b = -S_w D_{gw} \tau^b \left(\rho_{gw} - \rho_{gw}^b\right) \tag{39}$$

$$i_{gw}^t = -S_w D_{gw} \tau^t \left(\rho_{gw} - \rho_{gw}^t\right) \tag{40}$$

where ρ_{gw}^b, ρ_{gw} and ρ_{gw}^t represent the mass concentration of gas species in the liquid phase at the bottom side, the mid-plane and the top side of the discontinuity, respectively, and τ^b and τ^t [1/m] are constant coefficients that account for the effect of the discontinuity geometry in the effective transversal diffusivities. These expressions are obtained under the assumption that the liquid phase density is constant across the discontinuity. As for the transversal fluid flows, the transversal diffusive flows are positive when they go into the discontinuity.

Finally, considering Henry's law (Eq. (8)) and assuming that the gas has an ideal behaviour, Eqs. (39) and (40) can be rewritten in terms of the normal gas pressure jumps (Eqs. (32) and (33)) as follows:

$$i_{gw}^b = -S_w D_{gw} \tau^b H \frac{\partial \rho_g}{\partial p_g} \check{p}_g^b \tag{41}$$

$$i_{gw}^t = -S_w D_{gw} \tau^t H \frac{\partial \rho_g}{\partial p_g} \check{p}_g^t \tag{42}$$

4.2.4. Liquid retention and relative permeability

Similarly to the continuum medium, the liquid retention of the discontinuity is also modelled with a van Genuchten curve. However, the assumption made for the continuum medium that the curve parameters will remain constant since the expected variation of the pore space is small is revised for discontinuities, where the 'pore' space filled with the fluid phases will vary dramatically with the normal aperture. In order to introduce this effect, Eq. (14) is rewritten in terms of functions $\bar{p}_b(r_n)$ and $\bar{S}_{wr}(r_n)$ instead of constant parameters p_b and S_{wr}, i.e.

$$S_w(p_c, r_n) = \left(1 - \bar{S}_{wr}\right)\left[1 + \left(\frac{p_c}{\bar{p}_b}\right)^{\frac{1}{1-\lambda}}\right]^{-\lambda} + \bar{S}_{wr} \tag{43}$$

Note that the parameter λ is still deemed a constant parameter.

In order to obtain functions $\bar{p}_b(r_n)$ and $\bar{S}_{wr}(r_n)$, two possible states of the discontinuity are considered: closed, when $r_n \leq 0$, and open, when $r_n > 0$. As stated in Section 2, one of the premises of the proposed modelling approach is that the interface elements representing potential cracking paths must not have any significant effect in the overall behaviour of the modelled material, as long as they remain closed. In other words, in closed state, the retention curve of the discontinuity must be the same as the one for the continuum medium. This implies that for $r_n \leq 0$, $\bar{p}_b = p_b$ and $\bar{S}_{wr} = S_{wr}$. In contrast, in the open state, the parameter $\bar{p}_b$, which is linked to the gas-entry value, and the parameter $\bar{S}_{wr}$, which accounts for the fraction of the discontinuity volume occupied by immobile (residual) liquid, is expected to decrease for increasing r_n.

In order to derive $\bar{p}_b(r_n)$ in the open state, first consider the Laplace equation to estimate the gas-entry value of the porous medium:

$$p_{ev} = T_s\left(\frac{1}{R_1} + \frac{1}{R_2}\right) \tag{44}$$

where T_s [N/m] is the liquid–gas interfacial tension, and R_1 and R_2 [m] are the curvature radii of the gas–liquid interface. Assuming that

$R_1 = R_2 = d/2$, a characteristic pore size of the porous medium can be obtained as $d = 4T_s/p_{ev}$. Likewise, the gas-entry value of an open discontinuity ($\bar{p}_{ev}$) is approximated with the same Laplace's equation, but with $1/R_1 = 0$ and $R_2 = d/4 + \bar{r}/2$, i.e.

$$\bar{p}_{ev} = \frac{2T_s}{d/2 + \bar{r}} = \frac{d}{d + 2\bar{r}} p_{ev} \tag{45}$$

where $\bar{r}$ [m] represents the effective aperture of the discontinuity. In a strict sense, $\bar{r}$ should be the positive part of r_n. However, in order to prevent numerical problems, $\bar{r}$ is obtained as follows:

$$\bar{r}(r_n) = \langle r_n \rangle - \alpha \left[1 - \exp\left(-\frac{\langle r_n \rangle}{\alpha} \right) \right] \tag{46}$$

where the third term gives C^1 continuity to the function $\bar{r}(r_n)$ and makes it possible to smooth the transition between closed ($r_n \leq 0$) and open ($r_n > 0$) states by increasing the positive parameter α. Then, by assuming that $\bar{p}_b$ will evolve in proportion to $\bar{p}_{ev}$, the first expression sought is obtained:

$$\bar{p}_b = \frac{d}{d + 2\bar{r}} p_b \tag{47}$$

The second expression sought ($\bar{S}_{wr}$) is obtained by assigning an initial volume of immobile liquid phase to the discontinuity in closed state, and assuming that this volume will not grow nor decrease if the normal aperture becomes positive. Considering the pore volume associated to the closed discontinuity is nd, where n is the porosity of the porous medium and d is the above defined characteristic pore size, the volume of immobile liquid phase is estimated as $S_{wr}nd$. Then, considering the updated 'pore' volume of the discontinuity will be $nd + \bar{r}$, the residual saturation degree of the discontinuity will evolve as follows:

$$\bar{S}_{wr} = \frac{nd}{nd + \bar{r}} S_{wr} \tag{48}$$

Finally, the relative permeabilities are obtained with the same expressions used for the continuum medium (Eq. (15)), but introducing in the expression of the effective saturation the effect of the normal aperture in the residual saturation as obtained from Eq. (48), i.e.

$$S_e = \frac{S_w - \bar{S}_{wr}}{1 - \bar{S}_{wr}} \tag{49}$$

The proposed retention and relative permeability functions are illustrated in Figs. 6 and 7, respectively, which show their evolution for increasing values of r_n. The parameters used were $n = 0.39$, $p_{ev} = 5.0$ MPa, $p_b = 10.0$ MPa, $S_{wr} = 0.20$, $\lambda = 0.56$, $\alpha = 3000$ nm, $n_w = 1.5$, and $n_g = 3.0$. These parameters were calibrated for $r_n = 0$ with experimental data from bulk Boom clay (Gonzalez-Blanco et al., 2016; Volckaert et al., 1995). A standard value of $T_s = 72.7$ mN/m corresponding to an air–water interface at 20 °C is adopted (Vargaftik et al., 1983).

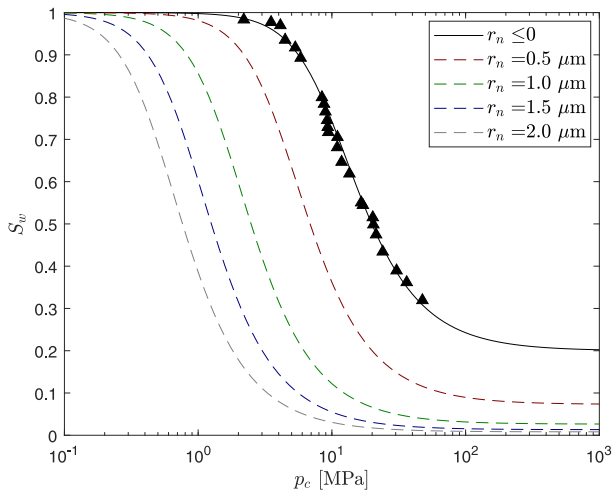

Fig. 6. Liquid retention curves for discontinuities in Boom clay with different normal aperture. The solid line corresponds to the bulk porous medium or a closed discontinuity ($r_n \leq 0$), while dashed lines correspond to discontinuities with increasing aperture ($r_n > 0$). Markers indicate experimental psychrometer measurements of intact Boom clay from Gonzalez-Blanco et al. (2016).

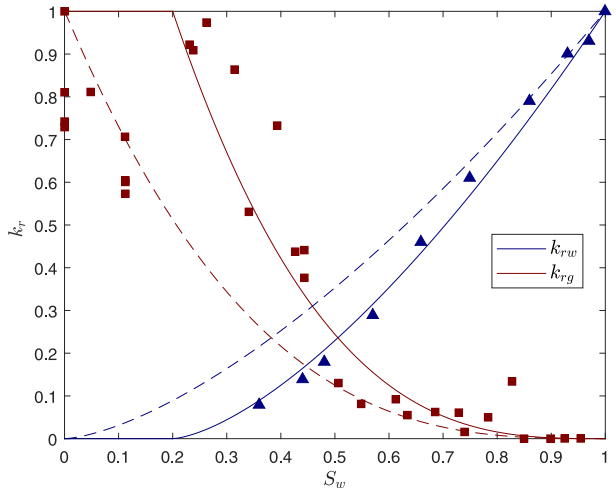

Fig. 7. Relative permeability functions for discontinuities in Boom Clay. Solid lines correspond to the bulk porous medium or a closed discontinuity ($r_n \leq 0$), while dashed lines correspond to a discontinuity with a large aperture ($r_n = 10$ μm). Markers indicate experimental data from Volckaert et al. (1995) for intact Boom Clay only.

5. Finite element implementation

The model outlined in the previous sections has been implemented in the FE code LAGAMINE. The porous medium equations have been discretised with a large strain element type, which is described in detail in Collin et al. (2002). This element has five degrees of freedom at each node (x and y coordinates, liquid pressure, gas pressure and temperature), though the temperature is fixed for the model proposed in this paper. The implementation of this element in LAGAMINE allows the use of shape functions of different order to interpolate the nodal displacements and pore pressures, in order to comply with the Ladyzhenskaya–Babuška–Brezzi stability condition (Brezzi and Bathe, 1990; Arnold, 1990). However, in the simulations performed for this paper the same parabolic shape functions has been used to interpolate displacements and fluid pressures, without observing spurious pressure oscillations or sub-optimal convergence behaviour. The nodal fluxes and forces are obtained after writing the integral forms of Eqs. (1), (4) and (5), and applying the Principle of Virtual Work (Collin, 2003). To increase the numerical stability, nodal water and gas flows, and the corresponding stiffness sub-matrices are always computed in the initial configuration. The so-called tangential stiffness matrix of the coupled element is monolithic, including all the coupling terms and second order effects due to geometry variation (Collin, 2003).

For the discontinuity equations, a new triple-node zero-thickness interface element has been formulated and implemented in LAGAMINE. The node numbering and nodal degrees of freedom are shown in Fig. 8 for a quadratic element. Note that the outer nodes (labelled t and b) are considered for both the mechanical and the flow problems, while the inner nodes (labelled m) are only considered for the flow problem. The FE formulation of the mechanical problem is developed with an updated Lagrangian approach and with a node-to-node discretisation of the contact area, by adapting the formulation outlined in Lequesne (2009) for purely mechanical double-node interface elements. In contrast to small displacement formulations where the normal and tangential components of the relative displacements and stresses are obtained with regard to the original configuration, in the proposed update Lagrangian

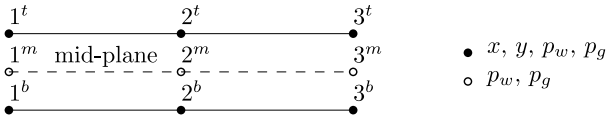

Fig. 8. Element node numbering and nodal degrees of freedom.

approach the position of the mechanical mid-plane, on which the local basis is defined, is updated in each loading increment. For this reason, the proposed element is suitable for problems in which the interface nodes experience large displacements and rotations, although with small relative displacement between opposite nodes of the same interface because of the node-to-node discretisation of the contact area.

The flow part of the FE formulation has been developed by adapting the coupled HM (single phase) formulation for double-node interface elements proposed in Segura and Carol (2004, 2008b). In double-node element formulations, the pressure inside the discontinuity is not considered as an independent degree of freedom but assumed to be the average between the pressure at the bottom and top faces. In Appendix A, it is demonstrated that the accuracy of this assumption depends mainly on the longitudinal fluid pressure profiles and the current values of the longitudinal and transversal hydraulic/diffusion coefficients, which in turn depends on the discontinuity mechanical aperture and the capillary pressure. It is concluded from this analysis, that the error introduced by the average pressure assumption used for double-node elements cannot be estimated a priori. Therefore, developing a triple-node element was preferred to be on the safe side, although at the expense of increasing the computational cost of the model. Moreover, triple-node elements outperform double-node ones in that they allow the user to hydraulically disconnect the continuum medium at one or both sides of the element from the discontinuity channel, just by nullifying the corresponding transversal hydraulic coefficients. In that way, triple-node elements are particularly well-suited for modelling hydraulic interfaces between a permeable medium and an impervious one, e.g. the interface between a clay sample and a metallic testing device. As with the continuum elements, in the proposed interface element the fluid pressure gradients are always computed in the initial configuration.

More comprehensive details of the formulation of the new interface element are presented in Appendix B.

Finally, after assemblage of the continuum and interface element nodal forces and mass fluxes, the mechanical equilibrium and mass balance with the imposed external forces/fluxes is enforced at the end of each time increment, i.e. adopting a backward Euler time integration scheme, using the standard Newton–Raphson Method.

The implementation in LAGAMINE of the new interface element and the corresponding constitutive laws has been systematically verified in simple benchmark problems with analytical solutions. A thorough verification of the continuum part of the model can be found in Collin (2003).

6. Model performance

In this section, the model performance is illustrated with some benchmark examples of increasing complexity. These examples were selected to show the main characteristics of the new PHM interface element and its ability to qualitatively reproduce experimental observations. A quantitative validation is not possible at the present state of development of the model due to the following reasons:

- Experiments are generally 3D and the current model implementation is 2D. The axisymmetry assumption, commonly used to model gas injection tests under oedometric or triaxial conditions, is not valid for the proposed modelling approach. Note that under the axisymmetry assumption 2D vertical/subvertical interface elements would represent cylindrical/conical cracks.
- The Dilatancy Controlled Gas Flow (Fig. 1, iii) is not yet implemented and, therefore, the contribution of this transport mechanism cannot be properly considered.
- Uncertainties/heterogeneities can cause a wide range of responses for the same experimental conditions. Such uncertainties/heterogeneities are not yet implemented in the model. Moreover, as discussed in the Introduction, only models explicitly accounting for the material heterogeneity seem to be able to reproduce preferential gas flow pathways in the bulk material.

These features are planned to be incorporated in future versions of the model.

In all the following benchmark examples, the gas species considered is hydrogen and the system temperature is $T = 298.15$ °K. Therefore, the following parameters of the fluid phases/species are common to all the examples: $M_g = 0.002$ kg/mol, $H = 0.0193$ (Sander, 2015), $D_{gw} = 5.25\times 10^{-9}$ m^2/s, $\rho_{w,o} = 997$ kg/m^3, $p_{w,o} = 0.1$ MPa, $C_w = 3.33\times 10^{-10}$ 1/Pa, $\mu_w = 8.9\times 10^{-4}$ Pa s (Haynes, 2014), and $\mu_g = 8.92\times 10^{-6}$ Pa s (Haynes, 2014). In the examples where the continuum medium is considered, plain strain is assumed and the following material parameters, representative of Boom clay, are used: $E = 300$ MPa (Volckaert et al., 2004), $\nu = 0.125$ (Volckaert et al., 2004), $n = 0.39$ (Mertens et al., 2004), $C_s \approx 0$, $b = 1$, $\mathbf{k} = 3\times 10^{-19}\mathbf{I}_2$ m^2 (Arnold et al., 2015) ($\mathbf{I}_2$ is the 2×2 identity tensor), and $\tau = 0.164$ (Jacops et al., 2013). Unless otherwise stated, the liquid retention and relative permeability parameters of the continuum medium and the discontinuities are the same as given in Section 4.2.4 for Figs. 6 and 7.

6.1. Gas injection in a single interface element

For the first two examples, a single interface element of 1 m length is considered. The displacements of the bottom face of the element are fixed, while a uniform compressive normal load $\sigma_{ini} = -0.4$ MPa is applied on the top face. The initial fluid pressures in all element nodes are $p_w = p_g = 0.1$ MPa. In both examples, gas is injected in the mid-plane nodes, while keeping constant the liquid phase pressure.

6.1.1. Case A

In this example, gas is injected at a constant mass rate of 0.1 μg/s. The parameters of the mechanical constitutive law are such that the interface behaves linear-elastically with a normal stiffness $K_n = 1\times 10^{12}$ Pa/m during the injection. Damage is prevented by adopting a large value of r_{n0}. Moreover, no viscosity is considered ($\zeta = 0$). Since there is no tangential loading and the pore pressure only acts in the normal direction, the tangential mechanical parameters are irrelevant. The integration points are considered in coincidence with the mid-plane nodes (Lobatto quadrature). In order to prevent longitudinal fluxes, the gas injection is distributed between the three mid-plane nodes according to the weights of the integration points at the same location.

Fig. 9 shows the time evolution of selected model variables as gas is injected. The curves are shifted along the time axis to make more visible the values at the beginning of the injection. Initially, the normal aperture is slightly negative ($r_n = -0.3$ μm) due to the compressive load. However, the initial width is positive because $w_0 = 1$ μm has been adopted. In this way, an initial storage capacity is assigned to the element, which prevents a sudden increase of the gas pressure and the normal aperture in the first time increment.

As gas is injected, the effective pore pressure grows monotonically as well as the normal aperture. Both curves hold a proportionality factor of $1/K_n$. The gas pressure, in contrast, shows a non-monotonic evolution, with a local peak when the normal aperture becomes positive. This peak is explained by the marked effect of the (positive) normal aperture on the retention curve by reducing the gas-entry value (Fig. 6). As the saturation degree tends to zero, the gas pressure curves converge to the effective pore pressure curve. Note that even when the saturation degree remains practically constant at $S_w \approx 0$, the relation

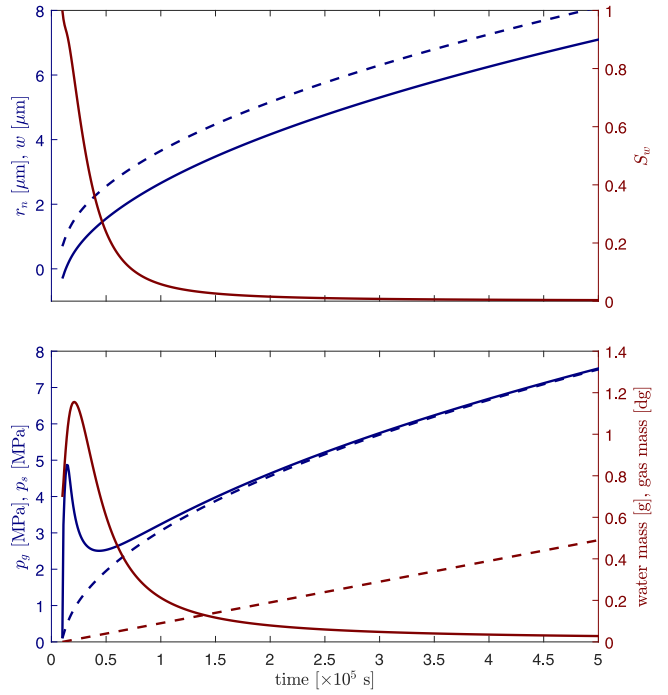

Fig. 9. Case A – Time evolution of the normal aperture r_n, the width w (dashed line), the liquid saturation degree S_w, the gas phase pressure p_g, the effective pore pressure p_s (dashed line), and the stored water and gas (dashed line) masses.

between the increments of gas pressure and the increments of aperture is still non-linear due to the compressibility of the gas phase.

The constant injection rate is reflected in the linear increase of the stored gas mass. The stored water mass curve, in contrast, shows a peak that is explained by the competing effects of the reduction of S_w and the increase of r_n on the storage term of the water mass balance equation. Initially, the positive effect of the increase of r_n overcomes the negative effect of the decrease of S_w and water enters the crack, but this behaviour rapidly reverted after the gas pressure peak, and, from then on, water is expelled.

Fig. 10 shows the equilibrium path in terms of p_g versus r_n as obtained numerically (markers) and analytically (solid lines). The analytical solution is given by the following implicit expression derived from Eqs. (17), (18) and (3):

$$\sigma_n'(r_n) + p_c S_w(r_n, p_c) - p_g = \sigma_{ini} \tag{50}$$

Keep in mind that in this case p_w is fixed, and σ_n' has been reduced to a function of r_n only, since no tangential displacements are possible. This expression has been plotted in Fig. 10 for three different values of α, in order to show the effect of the second term of Eq. (46) on the equilibrium path. Note that for very small or null values of α a sharp peak is obtained at $r_n = 0$. The dashed line in the plot has a slope K_n and reflects the linear elastic response of the interface element to the effective pore pressure. As the interface element is desaturated, the equilibrium path tends to this line.

Note that although the cracking process will not be modelled using a linear-elastic constitutive law, this example and the following one are representative of the conditions under which an interface element without (or with low) tensile strength will open when confined by linear-elastic continuum elements.

6.1.2. Case B

In this second example, the gas pressure is increased with a constant rate of 3.7×10^{-5} MPa/s until reaching $p_g = 7$ MPa, and then it is reduced, with the same rate, to the initial value.

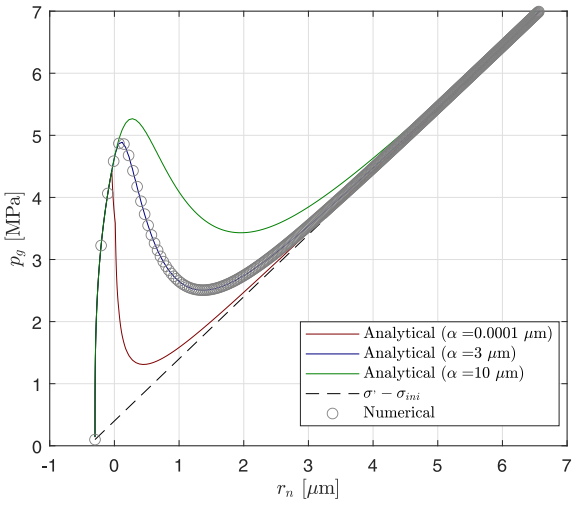

Fig. 10. Case A – Analytical equilibrium paths for different values of the aperture smoothing parameter α and numerical result for $\alpha = 3$ µm.

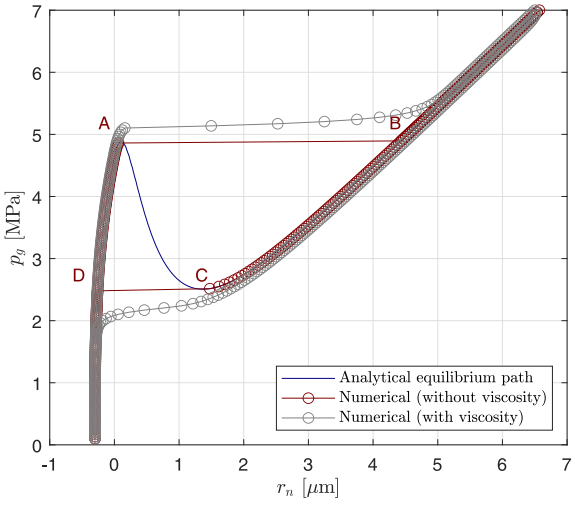

Fig. 11. Case B – Gas pressure versus normal aperture with and without adding viscous damping to the mechanical constitutive law. The blue line is the analytical equilibrium path obtained with Eq. (50).

In Fig. 11, the red curve shows the model results in terms of p_g versus r_n using the same mechanical parameters as in previous Case A. The blue curve corresponds to the equilibrium path calculated with Eq. (50), which is still valid for this case. As the gas pressure is increased, the normal aperture increases following the equilibrium path until reaching the local peak (point A). At this point, a sudden aperture occurs (snap-through instability) until reaching point B on the equilibrium path. Here on, further increase of the gas pressure leads to further normal aperture increase, following the equilibrium path until reaching $p_g = 7$ MPa. The subsequent reduction of the gas pressure is accompanied by the closure of the interface following the equilibrium path until reaching point C, where another aperture jump occurs until reaching the equilibrium path at point D. The initial (negative) aperture is recovered when the gas pressure reaches its initial value $p_g = 0.1$ MPa.

Snap-through instabilities of the type observed in this example (A→B and C→D), which in this case are properly handled by the iterative solving algorithm, have been found to lead to severe convergence problems in more complex boundary value problems. This occurs even when the gas injection is done at a controlled mass rate, because the

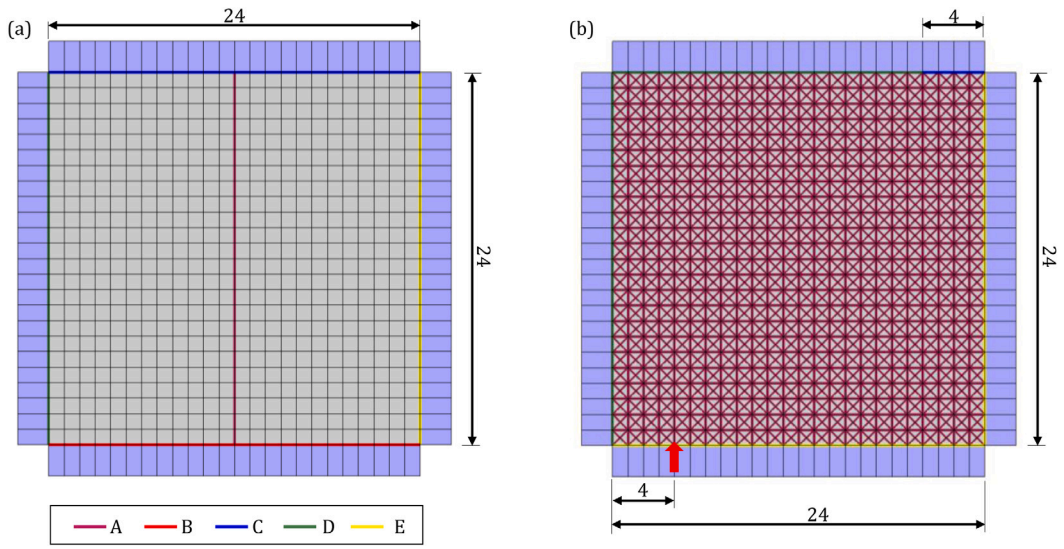

Fig. 12. Geometry and FE mesh for (a) Case C and (b) Case D. Thick lines indicate the location of the interface elements. The red arrow in (b) indicates the gas injection locus. Dimensions in mm.

gas accumulated (stored) in the system may act as a pressure buffer at the mouth of the opening crack.

One possibility to mitigate this problem is to increase the smoothing parameter α in order to reduce or eliminate the local peak of the equilibrium path, as illustrated in Fig. 10. Alternatively (or simultaneously), the viscous damper proposed in Eq. (25) can be activated. The grey curve in Fig. 11 shows the stabilising effect of the viscous term with $\zeta = 2 \times 10^5$ Pa s/m. Both numerical parameters α and ζ are tuned by trial and error. Since they introduce a deviation from the intended constitutive behaviour, they should be as small as possible.

6.2. Gas injection in a clay sample

6.2.1. Case C

This example aims at mimicking, in a simplified manner, a gas injection test in a water saturated clay sample under isochoric conditions. The problem geometry and the FE mesh considered are depicted in Fig. 12a. A square sample of Boom Clay is placed in between four stiff loading plates. The thicker lines labelled A–D indicate the position of the interface elements. A single, vertical crack propagation path is considered inside the sample (line A). The contact surfaces between the sample and the loading plates are represented by interface elements along lines B, C and D.

The initial stress state of the continuum clay elements is isotropic, with a total stress of −4.5 MPa. The initial stress state of all the interface elements is given by $\sigma_n = -4.5$ MPa and $\sigma_l = 0$. The initial pore pressures in all the domain is $p_w = p_g = 2.2$ MPa. All the degrees of freedom of the nodes belonging to the loading plates are fixed. Gas is injected at a constant mass rate of 1 μg/s, evenly distributed among all the mid-plane nodes of the interface elements along line B (Fig. 12a). The gas injection is performed in two stages of 0.6 Ms (1 Ms = 1×10^6 s), with a third stage of 0.6 Ms without injection in between. Time steps range between 1 to 5000 s, governed by an automatic incrementation algorithm.

The mechanical and flow properties of the clay continuum elements are those given at the beginning of the section. The material parameters of the loading plates continuum elements are irrelevant, since all their nodal degrees of freedom are fixed. The flow and mechanical parameters for the different lines of interface elements are given in Table 1. The mechanical parameters of the elements along line A have been estimated in an attempt to make them representative of Boom clay fracture properties, although the data available in this regard is very sparse. The initial tensile strength and the debonding normal aperture are adopted based on experimental direct tensile tests reported in the literature for different clayey soils (Trabelsi et al., 2018; Wang et al., 2007; Tang et al., 2015). To the best of the authors' knowledge no direct tensile tests on Boom clay have been reported. Because the adopted mechanical constitutive law is purely cohesive, the increase of shear strength with the confining stress due to friction is not automatically considered. In order to approximate this behaviour, the initial shear strength has been estimated considering the Mohr–Coulomb failure criterion with typical Boom clay values of $c' = 0.5$ MPa and $\varphi' = 18°$ (Arnold et al., 2015), and an average effective normal stress of 4.5 MPa during the injection (obtained from preliminary simulations). The initial tensile and shear strength of the clay–plate interfaces (lines B, C and D) are assumed to be a tenth of the corresponding values of the bulk clay (line A). In order use the same penalty coefficients as for line A, the cracking separations (r_{n0}, r_{l0}) are also reduced to a tenth. The snap-through instabilities described in Section 6.1.2, are prevented by assigning a viscosity $\zeta = 3 \times 10^{14}$ Pa s/m to line A elements.

In addition to representing the mechanical clay–plate interface, lines B and C are also used to simulate the porous filter on top and bottom sides of the sample. With this purpose, non-null values w_0, t_0^l and d_0^l have been assigned to them in order to consider the storage capacity and the high permeability/diffusivity of the filters. Moreover, at the gas injection side (line A) the liquid saturation degree has been fixed to $S_w = 0$, while at the back-pressure side full liquid saturation is enforced ($S_w = 1$). Note that because of the adopted transversal transport properties, the bottom and lateral plates are hydraulically disconnected from the clay sample.

The liquid retention parameters of lines A, D and E are the same as used for Fig. 6, with the exception of the first (bottom) element of line A, where the parameter p_b has been reduced to 1 MPa. This reduction of the gas-entry value is used to represent an imperfection at the sample bottom surface (a void or a cleft), where water can be displaced with lower capillary pressure than in the bulk clay. Otherwise, the gas pressure front would advance homogeneously into the sample precluding the formation of a crack. According to the discussion in Section 4.2.4, the reduction of p_b from 10 to 1 MPa, corresponds to an increase of the characteristic pore size from 58.1 nm to 581 nm. Pore size density functions obtained via Mercury Intrusion Porosimetry on Boom clay samples (Gonzalez-Blanco et al., 2016) show that features in the order of 500 nm are not unlikely.

Fig. 13 shows the time evolution of selected model variables. The gas injection pressure corresponds to the gas phase pressure of the mid-plane nodes of the elements along line B. Because of the high value

Table 1
Material parameters of the interface elements in Cases C and D (Fig. 12). The local longitudinal axes of the interface elements are oriented from left to right or from bottom to top.

	Line A	Line B	Line C	Line D	Line E
w_0 [m]	0.0	1.0E−5	1.0E−5	0.0	0.0
r_0^l [m^3]	0.0	1.0E−16	1.0E−16	0.0	0.0
k^b; k^t [m]	1.0E−6; 1E−6	0.0; 1E−6	1.0E−6; 1.0E−6	1.0E−6; 0.0	0.0; 1.0E−6
d_0^t [m]	0.0	1E−05	1E−05	0.0	0.0
τ^b; τ^t [1/m]	1.0; 1.0	0.0; 1.0	1.0; 1.0	1.0; 0.0	1.0; 0.0
σ_{n0} [Pa]	1.5E+5	1.5E+4	1.5E+4	1.5E+4	1.5E+4
r_{n0}; r_{nc} [m]	1.5E−9; 1.5E−4	1.5E−10; 1.5E−5	1.5E−10; 1.5E−5	1.5E−10; 1.5E−5	1.5E−10; 1.5E−5
σ_{l0} [Pa]	2.0E+6	2.0E+5	2.0E+5	2.0E+5	2.0E+5
r_{l0}; r_{lc} [m]	2.0E−8; 2.0E−3	2.0E−9; 4.0E−4	2.0E−9; 2.0E−4	2.0E−9; 2.0E−4	2.0E−9; 1.0E−4

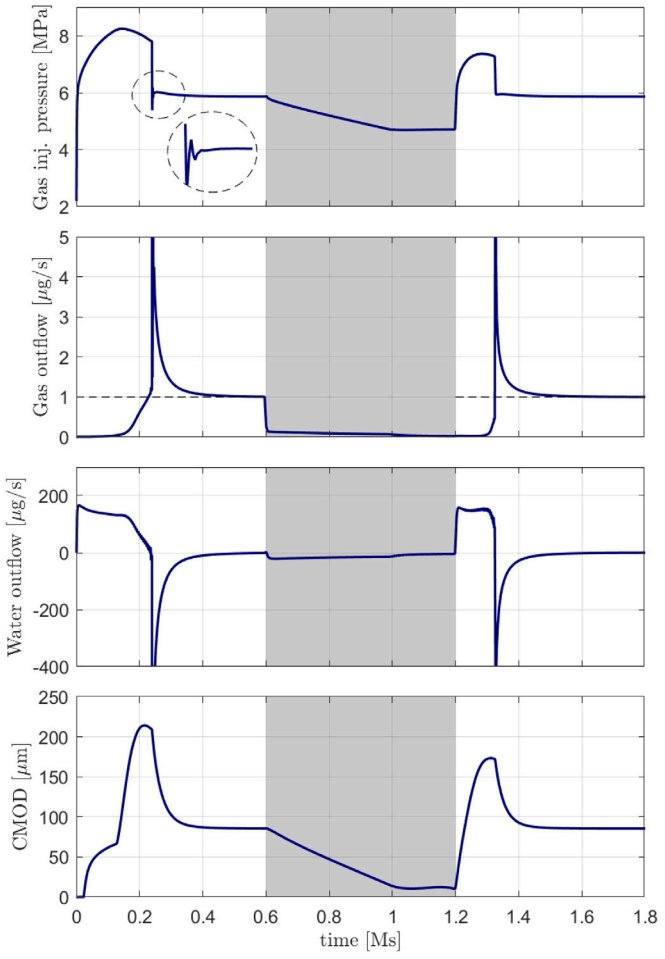

Fig. 13. Case C – Time evolution of the gas injection pressure, the gas and water mass outflows, and the Crack Mouth Opening Displacement (CMOD).

of r_0^l, the gas pressure at all these nodes is practically the same. The Crack Mouth Opening Displacement (CMOD) is the normal aperture of the first interface element along line A. The gas and water outflows correspond to the mass rates at which a gas and water species leave the clay sample through the top boundary. A negative water outflow indicates that water is being absorbed by the sample. These curves are complemented by Fig. 14, which shows the deformed geometry and contour plots of gas phase pressure, liquid phase pressure and liquid saturation degree at four characteristic times, namely, when the maximum injection pressure is reached (0.15 Ms), just before and just after the crack reaches the top plate (0.236 and 0.24 Ms), and at the end of the first injection stage (0.6 Ms).

Between the beginning of the injection and time 0.15 Ms, the gas injection pressure grows monotonically until reaching its maximum value. This pressure increase is accompanied by a separation of the bottom side interface, which occurs at the expense of compressing the clay sample against the top and lateral loading plates, inducing shear stress/displacements along the lateral interface elements. Part of the gas injected during this period is accumulated in the void volume created in that way, while the remaining part invades the clay sample. The gas invasion occurs both into the pore space of the bulk clay (dissolved in the pore water and as a separate phase) and into the crack induced by the gas pressure. The progressive decline of the injection pressure rate is mainly explained by the propagation of the crack, which increases the storage capacity and the overall permeability of the clay sample. The 'room' necessary for the formation of the crack and the separation of the bottom side interface is created by reduction of the pore space in the bulk clay material in a consolidation process accompanied by water expulsion.

After the peak, the injection pressure progressively decreases until time 0.236 Ms, when the crack reaches the top plate and a sudden pressure drop occurs. At this time, the crack connects the injection locus at the bottom of the sample with the gas sink at the top, constituting a preferential path for gas flow. Consequently, a sharp raise of the gas outflow is observed, mainly fed by gas previously stored in the bottom contact interface and in the crack. Qualitatively similar sharp break-through events were experimentally observed by Horseman et al. (1999), Graham et al. (2016), Daniels and Harrington (2017), Harrington et al. (2017, 2019) and Gutiérrez-Rodrigo et al. (2021).

Because of the gas pressure drop, the bulk clay is decompressed and partially re-saturated, as it is reflected in the negative values of the water outflow curve. The gas and water outflow extreme values are far out of the plotted ranges, reaching values of 8×10^{-8} and -16×10^{-7} kg/s, respectively. After this first break-through event, the system goes through a cycle of damped oscillations before smoothly converging to a steady state as the gas outflow converges to the injection rate value. These oscillations are highlighted in the injection pressure plot, but they can also be observed in the gas and water outflow plots. From the mechanical point of view, the oscillations are associated to partial closure and reopening of the crack tip. Notably, oscillatory or intermittent outflows after break-through events are also observed experimentally (Graham et al., 2016; Daniels and Harrington, 2017; Harrington et al., 2017, 2019). Moreover, a detailed analysis of stress perturbation events indicates that the intermittent outflows are correlated with the opening and closing of cracks (Harrington et al., 2019).

The injection shut-off at time 0.6 Ms, leads to a decrease of the gas pressure at the injection locus as gas continues flowing out of the sample through the top side. The gas pressure decrease is accompanied by the progressive closure of the crack. At time 1.0 Ms, when the gas injection pressure reaches $p_g \approx |\sigma_{ini}| = 4.5$ MPa, the crack is almost completely closed and, consequently, the dissipation of the gas overpressure slows down significantly, driven only by the gas transport processes in the continuum elements. Self-sealing of gas pathways following reduction of the injection rate/pressure has been reported in different gas migration tests by Horseman et al. (1999), Graham et al.

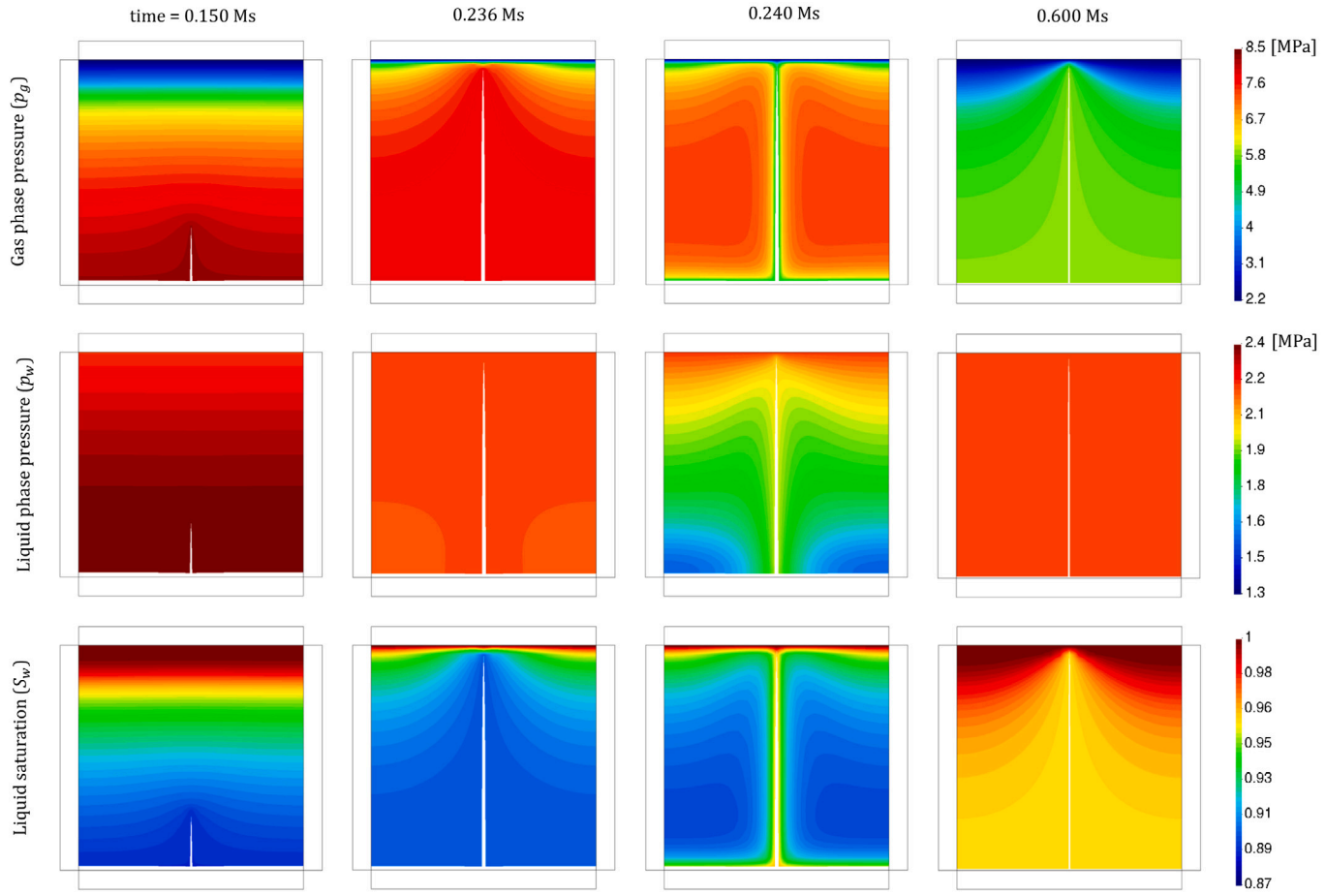

Fig. 14. Case C – Deformed geometry (scaled ×2), gas phase pressure, liquid phase pressure, and liquid saturation degree at four characteristic times.

(2016), Daniels and Harrington (2017), Harrington et al. (2019) and Gutiérrez-Rodrigo et al. (2021).

At time 1.2 Ms, the gas injection is restarted. In this second injection stage, the evolution curves show similar features to that of the first stage, although with some significant differences. Namely, the maximum injection pressure and the time required to connect the bottom and top plates with the crack are smaller, and the oscillations after the break-through event practically disappear. These differences are attributed to the fact that the initial conditions are different in each case. On one hand, the gas overpressure resulting from the first injection is not completely dissipated during the shut-off stage, and, therefore, less injection time is needed in the second injection stage to reach critical pressure values. On the other hand, the interface elements along lines A, B, D and E offer less or no resistance to opening/sliding during the second injection, since they have been damaged during the first injection stage. Comparable reduction of the break-through pressure in second injections was systematically observed in tests conducted by Gutiérrez-Rodrigo et al. (2021) in compacted bentonite.

This example makes it possible to appreciate the enrichment of the conventional PHM FE model for bulk clay by the introduction of the new zero-thickness interface elements for representing both macroscopic cracks inside the clay specimen and the distinct behaviour of the interfaces between the specimen and the experimental testing device. Now, in addition to the diffusion/advection of dissolved gas and the two-phase flow mechanisms of the original model, the new model is capable of automatically activating the gas fracturing mechanism when the conditions are met. Moreover, the explicit representation of the clay–device interfaces, which is not possible with any of the modelling approaches reviewed in the introduction, reveals that actual boundary conditions of the clay specimens during gas injection tests may differ significantly from the nominal ones.

6.2.2. Case D

This example aims at demonstrating the ability of the model to reproduce non-straight and branching cracking paths. For this purpose, a similar problem definition as for Case C is considered, but using a different FE mesh and introducing changes in the flow boundary conditions. The new FE mesh is shown in Fig. 12b, where the labels of the interface element lines correspond to the material parameters given in Table 1. Note in that figure, that the back-pressure filter has been reduced to 1/6 of the top side length of the sample (line C in Fig. 12b), the bottom injection filter has been removed, and that interface elements have been introduced in between all the continuum clay elements. The gas injection is performed with the same mass rate as for Case C (1 μg/s), but at a single mid-plane node indicated by a red arrow in Fig. 12b, instead of uniformly distributed along the bottom side of the sample. Additionally, in order to reduce the computational cost, the liquid pressure is fixed in all the domain.

Since the crack can propagate only along the interface elements, the discretisation of the sample will determine the potential cracking paths and, consequently, the geometric characteristics of the FE mesh will have an influence on the results. In order to explore the mesh sensitivity of the proposed example, the simulation is repeated using three other FE meshes shown in Fig. 15. The notation of the meshes indicates the number of elements along one side of the sample, and the structured (s) or unstructured (u) nature of the mesh. Mesh 24s is the same mesh

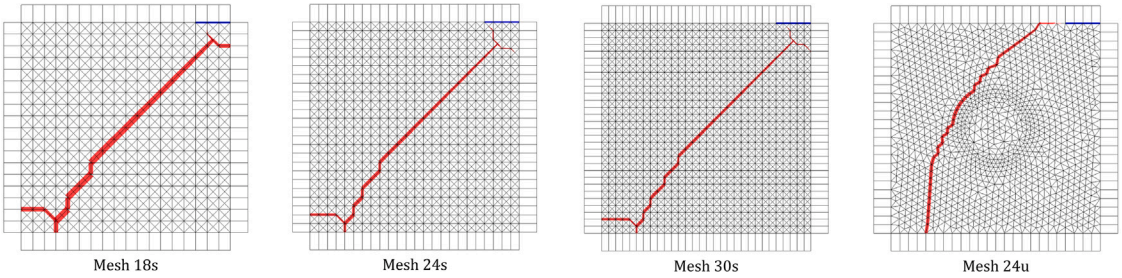

Fig. 15. Case D – FE meshes considered for sensitivity analysis. The red lines represent the crack geometry at the end of the simulation. The varying thickness of the lines corresponds to the normal crack aperture (r_n) magnified by ×5.5. The blue segment indicates the position of the gas sink.

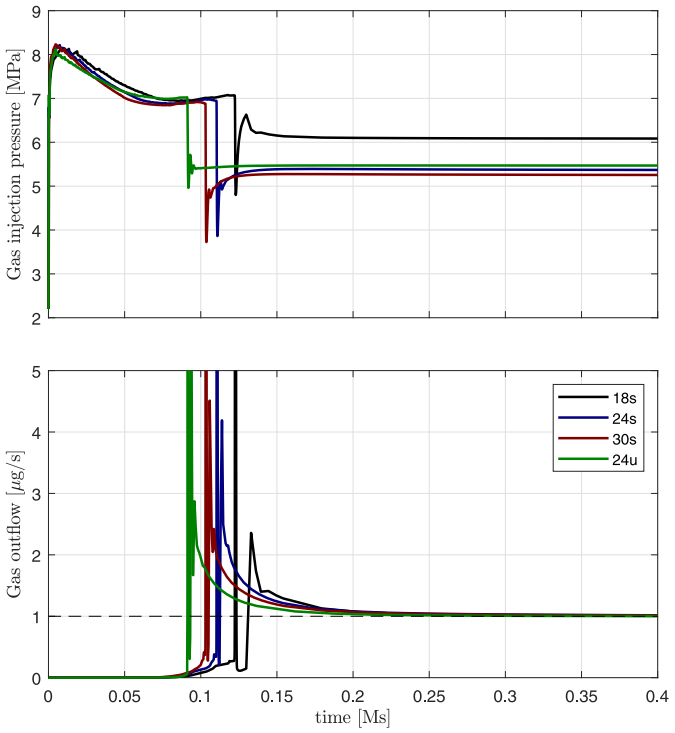

Fig. 16. Case D – Time evolution of the gas injection pressure and the gas mass outflow obtained with four different FE meshes.

shown in Fig. 12b. Mesh 24u was obtained by forcing a circular mesh line in the centre of the sample.

The results obtained are presented in Fig. 16 in terms of the time evolution of the gas injection pressure and the gas mass outflow through the back-pressure filter. The crack geometry at the end of the simulation is shown in Fig. 15 for the four different FE meshes considered.

The value and time of the injection pressure peaks are very similar with the four different meshes. This peak corresponds to the initiation of the crack propagation into the sample. The effect of the mesh can only be appreciated in the post-peak behaviour.

Consider first the structured meshes 18s, 24s and 30s. Although the final crack geometry in the three cases are very similar (Fig. 15), it is apparent from the injection pressure curves, that the model response is 'embrittled' as the mesh size is reduced, in the sense that the crack reaches more rapidly the back-pressure filter. The coarser the mesh, the more unlikely that the optimal (minimum energy) cracking path can be accurately reproduced by the model, and, consequently, additional mechanical work needs to be invested to propagate the crack.

Compare now the results obtained with meshes 24s and 24u, which have similar element size, but one is structured and the other unstructured. Although the crack geometries obtained with these meshes are quite different, the time evolution curves of the injection pressure and gas outflow are very similar until well past the post-peak zone. The injection pressure curve of mesh 24u shows a similar drop when the crack reaches the back-pressure filter, but then it occurs 0.02 Ms before. This difference is explained (at least in part) by the fact that the last part of the crack propagation is developed along the top clay–plate interface, which has 1/10 of the tensile strength of the bulk material.

As for Case C, a cycle of oscillations in the gas injection pressure and outflow is obtained after the break-through event, for all four different meshes. These oscillations are associated to partial closure and reopening of the crack tip(s).

7. Conclusion

A model has been presented which aims at simulating gas migration in water saturated clay. This model extends a pre-existing two-phase two-species HM model for bulk porous media in order to explicitly represent existing or potential discontinuities by means of zero-thickness interface elements. For this purpose, a new PHM triple-node zero-thickness interface element has been developed. The model is now able to simultaneously simulate the diffusion and advection of dissolved gas and the displacement of the liquid phase filling the clay pores by the invading gas, together with the localised gas flow along macroscopic cracks induced and propagated by the gas pressure.

The model advances the state of the art by having the following characteristics:

- The explicit representation of the PHM behaviour of sample–device interfaces.
- The initiation and propagation of macroscopic gas cracks inside the water saturated bulk material.
- The modification of the flow patterns inside the bulk material as a consequence of the localised flows along the cracks.
- The sharp drop of the gas injection pressure when the gas crack reaches the back-pressure filter, followed by some fluctuations before reaching a steady state.
- The closure (self-sealing) of the gas cracks when the gas injection ceases.

With these advances, the proposed model configures a powerful tool to assess/explore the effect of induced cracks and sample–device interfaces on the migration gas in saturated clay.

Nonetheless, further developments are still necessary to allow a quantitative validation of the model, e.g. implementation of the pathway dilation mechanism, introduction of variability/heterogeneity of the material properties, and extension to 3D. Moreover, in order to reduce the computational cost of the proposed modelling approach, a new numerical strategy would be advantageous to introduce (or activate previously introduced) interface elements only where/when they are needed to represent the formation of cracks.

CRediT authorship contribution statement

Joaquín Liaudat: Conceptualization, Methodology, Software, Validation, Writing – original draft. **Anne-Catherine Dieudonné:** Conceptualization, Supervision, Funding acquisition, Project administration, Writing – review & editing. **Philip J. Vardon:** Conceptualization, Supervision, Funding acquisition, Project administration, Writing – review & editing.

Declaration of competing interest

The authors declare that they have no known competing financial interests or personal relationships that could have appeared to influence the work reported in this paper.

Data availability

No data was used for the research described in the article.

Acknowledgements

This paper was performed in the framework of the European Joint Programme on Radioactive Waste Management (EURAD). EURAD has received funding from the European Union's Horizon 2020 research and innovation programme under grant agreement No. 847593. Additional funding from COVRA, The Netherlands for this work is gratefully acknowledged. The first author has received funding from the European Union's Horizon 2020 research and innovation programme under the Marie Skłodowska-Curie grant agreement No. 101028292.

Appendix A. Double- and triple-node interface elements

The formulation of double-node interface elements is developed under the assumption that the fluid pressure inside the discontinuity is approximately equal to the average between top and bottom face pressures, i.e.

$$p_\pi \approx \frac{p_\pi^b + p_\pi^t}{2} \tag{A.1}$$

In order to assess the validity of this assumption, let us consider the mass balance Eqs. (26) and (27) for a steady state:

$$\frac{\partial q_\varsigma^l}{\partial l} - q_\varsigma^b - q_\varsigma^t = 0 \quad \text{for } \varsigma = \mathrm{w}, \mathrm{g} \tag{A.2}$$

Introduction of Eqs. (29)–(34) in this expression leads to:

$$\frac{\partial}{\partial l}\left(\rho_\pi T_\pi^l \frac{\partial p_\pi}{\partial l}\right) - \rho_\pi K_\pi^t \left(p_\pi - p_\pi^b\right) - \rho_\pi K_\pi^t \left(p_\pi - p_\pi^t\right) = 0 \quad \text{for } \pi = w, g \tag{A.3}$$

where $T_\pi^l = k_{\pi,r} t^l / \mu_\pi$ and $K_\pi^t = k_{\pi,r} k^t / \mu_\pi$. For the sake of simplicity, the gas dissolved in the liquid phase has been neglected and the bottom and top transversal hydraulic coefficients are assumed to be equal. Finally, after some algebra, the following expression is obtained:

$$p_\pi - \frac{p_\pi^b + p_\pi^t}{2} = \frac{T_\pi^l}{2K_\pi^t}\frac{\partial^2 p_\pi}{\partial l^2} + \frac{1}{2K_\pi^t}\frac{\partial T_\pi^l}{\partial l}\frac{\partial p_\pi}{\partial l} + \frac{T_\pi^l}{2K_\pi^t \rho_\pi}\frac{\partial \rho_\pi}{\partial p_\pi}\left(\frac{\partial p_\pi}{\partial l}\right)^2 \tag{A.4}$$

Note that the significance of the right hand side terms in this equation determines the accuracy of the average pressure assumption (Eq. (A.1)). From them, it can be concluded, that for a given longitudinal pressure profile, the difference between the results obtained with triple-node elements and the results obtained with double-node elements will be mainly determined by the longitudinal and transversal hydraulic conductivities T_π^l and K_π^t. The higher K_π^t and the lower T_π^l, the more similar the results obtained with both kinds of interface elements. A similar conclusion was drawn by Segura and Carol (2004) after comparing the performance of triple- and double-node elements for modelling water flow in a discontinuous medium.

Appendix B. Interface element formulation

Nodal unknowns

The nodal unknowns vector $\bar{\mathbf{u}}$ of the interface element depicted in Fig. 8 is defined as follows:

$$\bar{\mathbf{u}} = \begin{bmatrix} \bar{\mathbf{x}} \\ \bar{\mathbf{p}}_w \\ \bar{\mathbf{p}}_g \end{bmatrix} \text{with } \bar{\mathbf{x}} = \begin{bmatrix} \bar{\mathbf{x}}^b \\ \bar{\mathbf{x}}^t \end{bmatrix} \text{ and } \bar{\mathbf{p}}_\pi = \begin{bmatrix} \bar{\mathbf{p}}_\pi^b \\ \bar{\mathbf{p}}_\pi^t \\ \bar{\mathbf{p}}_\pi^m \end{bmatrix} \tag{B.1}$$

where vectors $\bar{\mathbf{x}}$ and $\bar{\mathbf{p}}_\pi$ ($\pi = w, g$) store the nodal coordinates, liquid phase pressures and gas phase pressures, respectively. The superindexes b, t, and m indicate if the nodes correspond to the bottom face, top face or mid-plane of the element. The components of the unknowns vectors are the following:

$$\bar{\mathbf{x}}^b = \begin{bmatrix} x_1^b & y_1^b & x_2^b & y_2^b & x_3^b & y_3^b \end{bmatrix}^\mathsf{T} \tag{B.2}$$

$$\bar{\mathbf{x}}^t = \begin{bmatrix} x_1^t & y_1^t & x_2^t & y_2^t & x_3^t & y_3^t \end{bmatrix}^\mathsf{T} \tag{B.3}$$

$$\bar{\mathbf{p}}_\pi^b = \begin{bmatrix} p_{\pi 1}^b & p_{\pi 2}^b & p_{\pi 3}^b \end{bmatrix}^\mathsf{T} \tag{B.4}$$

$$\bar{\mathbf{p}}_\pi^t = \begin{bmatrix} p_{\pi 1}^t & p_{\pi 2}^t & p_{\pi 3}^t \end{bmatrix}^\mathsf{T} \tag{B.5}$$

$$\bar{\mathbf{p}}_\pi^m = \begin{bmatrix} p_{\pi 1}^m & p_{2\pi}^m & p_{3\pi}^m \end{bmatrix}^\mathsf{T} \tag{B.6}$$

In addition to the independent nodal unknowns, dependent unknowns are defined for later convenience. The coordinates of the mid-plane nodes are obtained from the bottom and top coordinates as follows:

$$\bar{\mathbf{x}}^m = \frac{1}{2}\left(\bar{\mathbf{x}}^b + \bar{\mathbf{x}}^t\right) = \frac{1}{2}\begin{bmatrix} \mathbf{I}_6 & \mathbf{I}_6 \end{bmatrix} \bar{\mathbf{x}} \tag{B.7}$$

where $\mathbf{I}_6$ is the 6×6 identity matrix.

Similarly, the relative displacements between opposites nodes (in the global basis) are given by:

$$\bar{\mathbf{a}} = \bar{\mathbf{x}}^t - \bar{\mathbf{x}}^b = \begin{bmatrix} -\mathbf{I}_6 & \mathbf{I}_6 \end{bmatrix} \bar{\mathbf{x}} \tag{B.8}$$

Finally, the transversal pressure jumps between the bottom and top face nodes and the mid-plane nodes are obtained as follows:

$$\check{\mathbf{p}}_\pi^b = \left(\bar{\mathbf{p}}_\pi^m - \bar{\mathbf{p}}_\pi^b\right) = \begin{bmatrix} -\mathbf{I}_3 & \mathbf{0}_3 & \mathbf{I}_3 \end{bmatrix} \bar{\mathbf{p}}_\pi \tag{B.9}$$

$$\check{\mathbf{p}}_\pi^t = \left(\bar{\mathbf{p}}_\pi^m - \bar{\mathbf{p}}_\pi^t\right) = \begin{bmatrix} \mathbf{0}_3 & -\mathbf{I}_3 & \mathbf{I}_3 \end{bmatrix} \bar{\mathbf{p}}_\pi \tag{B.10}$$

where $\mathbf{0}_3$ and $\mathbf{I}_3$ are the 3×3 null and identity matrix, respectively.

Local basis

The local axes are defined along the mid-plane between the two discontinuity faces. The axis $\mathbf{e}_l$ is tangent to the mid-plane. The axis $\mathbf{e}_n$ is normal to $\mathbf{e}_l$. In addition, the isoparametric coordinate ξ is defined along the mid-plane such that its value is equal to -1 at the first node, 0 at the central node, and 1 at the last node.

Then, the local axes at a mid-plane point of coordinates $\mathbf{x}^m = \begin{bmatrix} x^m & y^m \end{bmatrix}^\mathsf{T}$ are given by:

$$\mathbf{e}_l = \frac{1}{|\mathbf{J}|}\frac{\partial \mathbf{x}^m}{\partial \xi} = \frac{1}{|\mathbf{J}|}\begin{bmatrix} \frac{\partial x^m}{\partial \xi} & \frac{\partial y^m}{\partial \xi} \end{bmatrix}^\mathsf{T} \tag{B.11}$$

$$\mathbf{e}_n = \frac{1}{|\mathbf{J}|}\begin{bmatrix} -\frac{\partial y^m}{\partial \xi} & \frac{\partial x^m}{\partial \xi} \end{bmatrix}^\mathsf{T} \tag{B.12}$$

with

$$|\mathbf{J}| = \sqrt{\left(\frac{\partial x^m}{\partial \xi}\right)^2 + \left(\frac{\partial y^m}{\partial \xi}\right)^2} \tag{B.13}$$

The global coordinates of the mid-plane point of isoparametric coordinate ξ are obtained from the global coordinates of the mid-plane nodes as follows:

$$x^m = \sum_{i=1}^{3} N_i(\xi) x_i^m; \quad y^m = \sum_{i=1}^{3} N_i(\xi) y_i^m \tag{B.14}$$

where $N_i(\xi)$ is the interpolation function of the mid-plane node i. Therefore,

$$\frac{\partial x^m}{\partial \xi} = \sum_{i=1}^{3} \frac{\partial N_i}{\partial \xi} x_i^m; \quad \frac{\partial y^m}{\partial \xi} = \sum_{i=1}^{3} \frac{\partial N_i}{\partial \xi} y_i^m \tag{B.15}$$

The local basis makes it possible to compute the components of relative displacement vector $\mathbf{r}$ from the global coordinates of the bottom and top faces with the following expressions:

$$r_n = \mathbf{e}_n \cdot \left(\mathbf{x}^t - \mathbf{x}^b\right) = \mathbf{e}_n \cdot \mathbf{a}; \quad r_l = \mathbf{e}_l \cdot \mathbf{a} \tag{B.16}$$

or with the following equivalent matrix form:

$$\mathbf{r} = \mathbf{R}\mathbf{a}, \text{ where } \mathbf{R} = \frac{1}{|\mathbf{J}|}\begin{bmatrix} \frac{-\partial y^m}{\partial \xi} & \frac{\partial x^m}{\partial \xi} \\ \frac{\partial x^m}{\partial \xi} & \frac{\partial y^m}{\partial \xi} \end{bmatrix} \tag{B.17}$$

Interpolation functions and matrices

The same interpolation functions N_i are employed for the mechanical and the hydraulic problems, namely:

$$N_1 = \frac{1}{2}\xi(\xi - 1); \; N_2 = \left(1 - \xi^2\right); \; N_3 = \frac{1}{2}\xi(\xi + 1) \tag{B.18}$$

With these functions the following interpolation matrices are constructed:

$$\mathbf{N}^x = \begin{bmatrix} N_1 & 0 & N_2 & 0 & N_3 & 0 \\ 0 & N_1 & 0 & N_2 & 0 & N_3 \end{bmatrix} \tag{B.19}$$

$$\mathbf{N}^p = \begin{bmatrix} N_1 & N_2 & N_3 \end{bmatrix} \tag{B.20}$$

These matrices are used as follows to interpolate the mid-plane coordinates, the relative displacements, the fluid pressures, and transversal pressure jumps, from the nodal unknown vectors $\bar{\mathbf{x}}$ and $\bar{\mathbf{p}}_\pi$:

$$\mathbf{x}^m = \mathbf{N}^x \bar{\mathbf{x}}^m = \frac{1}{2}\mathbf{N}^x \begin{bmatrix} \mathbf{I}_6 & \mathbf{I}_6 \end{bmatrix} \bar{\mathbf{x}} \tag{B.21}$$

$$\mathbf{r} = \mathbf{R}\mathbf{N}^x \bar{\mathbf{a}} = \mathbf{R}\mathbf{N}^x \begin{bmatrix} -\mathbf{I}_6 & \mathbf{I}_6 \end{bmatrix} \bar{\mathbf{x}} = \mathbf{B}^x \bar{\mathbf{x}} \tag{B.22}$$

$$p_\pi^m = \mathbf{N}^p \bar{\mathbf{p}}_\pi^m = \mathbf{N}^p \begin{bmatrix} \mathbf{0}_3 & \mathbf{0}_3 & \mathbf{I}_3 \end{bmatrix} \bar{\mathbf{p}}_\pi = \mathbf{B}^m \bar{\mathbf{p}}_\pi \tag{B.23}$$

$$\check{p}_\pi^b = \mathbf{N}^p \check{\mathbf{p}}_\pi^b = \mathbf{N}^p \begin{bmatrix} -\mathbf{I}_3 & \mathbf{0}_3 & \mathbf{I}_3 \end{bmatrix} \bar{\mathbf{p}}_\pi = \check{\mathbf{B}}^b \bar{\mathbf{p}}_\pi \tag{B.24}$$

$$\check{p}_\pi^t = \mathbf{N}^p \check{\mathbf{p}}_\pi^t = \mathbf{N}^p \begin{bmatrix} \mathbf{0}_3 & -\mathbf{I}_3 & \mathbf{I}_3 \end{bmatrix} \bar{\mathbf{p}}_\pi = \check{\mathbf{B}}^t \bar{\mathbf{p}}_\pi \tag{B.25}$$

The fluid phase pressure gradients along the mid-plane, which are required to compute the longitudinal mass flows of gas and water species, are obtained with the following expressions:

$$\frac{\partial p_\pi^m}{\partial l} = \frac{\partial \mathbf{B}^m}{\partial l} \bar{\mathbf{p}}_\pi \tag{B.26}$$

where

$$\frac{\partial \mathbf{B}^m}{\partial l} = \frac{1}{|\mathbf{J}|} \frac{\partial \mathbf{N}^p}{\partial \xi} \begin{bmatrix} \mathbf{0}_3 & \mathbf{0}_3 & \mathbf{I}_3 \end{bmatrix} \tag{B.27}$$

Nodal forces and mass flows

The nodal force and mass flow vector $\bar{\mathbf{f}}$ is defined as follows:

$$\bar{\mathbf{f}} = \begin{bmatrix} \bar{\mathbf{f}}_x \\ \bar{\mathbf{f}}_\mathrm{w} \\ \bar{\mathbf{f}}_\mathrm{g} \end{bmatrix} \tag{B.28}$$

The nodal force vector $\mathbf{f}_x$ [N] is obtained after applying the Principle of Virtual Work (PVW) to the integral form of Eq. (17):

$$\mathbf{f}^x = \int_{l_{mp}} (\mathbf{B}^x)^\top \boldsymbol{\sigma}' dl - \int_{l_{mp}} (\mathbf{B}^x)^\top \mathbf{m} p_s^m dl \tag{B.29}$$

Similarly, the nodal mass flows $\mathbf{f}_\varsigma$ [kg/s] ($\varsigma = \mathrm{w}, \mathrm{g}$) are obtained from the mass balance equations for water and gas species (Eqs. (4) and (5)):

$$\mathbf{f}_\varsigma = \int_{l_{mp}} (\mathbf{B}^m)^\top q_\varsigma^s dl - \int_{l_{mp}} \left(\frac{\partial \mathbf{B}^m}{\partial l}\right)^\top q_\varsigma^l dl - \int_{l_{mp}} \left(\check{\mathbf{B}}^b\right)^\top q_\varsigma^b dl - \int_{l_{mp}} \left(\check{\mathbf{B}}^t\right)^\top q_\varsigma^t dl \tag{B.30}$$

In this expression, q_ς^s stands for the mass storage rate of species ς, i.e. for the first terms in Eqs. (4) and (5).

The numerical integration of Eqs. (B.29) and (B.30) follows the Gauss' scheme with n_{ip} integration points:

$$\mathbf{f}_x = \sum_{i=1}^{n_{ip}} (\mathbf{B}^x)^\top \boldsymbol{\sigma}' |\mathbf{J}| W_i - \sum_{i=1}^{n_{ip}} (\mathbf{B}^x)^\top \mathbf{m} \mathbf{B}^m p_s^m |\mathbf{J}| W_i \tag{B.31}$$

$$\mathbf{f}_\varsigma = \sum_{i=1}^{n_{ip}} (\mathbf{B}^m)^\top q_\varsigma^s |\mathbf{J}| W_i - \sum_{i=1}^{n_{ip}} \left(\frac{\partial \mathbf{B}^m}{\partial l}\right)^\top q_\varsigma^l |\mathbf{J}| W_i - \sum_{i=1}^{n_{ip}} \left(\check{\mathbf{B}}^b\right)^\top q_\varsigma^b |\mathbf{J}| W_i - \sum_{i=1}^{n_{ip}} \left(\check{\mathbf{B}}^t\right)^\top q_\varsigma^t |\mathbf{J}| W_i \tag{B.32}$$

where W_i is the weight of the integration point i.

Tangent stiffness matrix

The numerical solution via a Newton–Raphson iterative strategy requires the computation of the following fully coupled tangent stiffness matrix:

$$\frac{\partial \bar{\mathbf{f}}}{\partial \bar{\mathbf{u}}} = \begin{bmatrix} \left.\frac{\partial \bar{\mathbf{f}}_x}{\partial \bar{\mathbf{x}}}\right|_{12\times12} & \left.\frac{\partial \bar{\mathbf{f}}_x}{\partial \bar{\mathbf{p}}_w}\right|_{12\times9} & \left.\frac{\partial \bar{\mathbf{f}}_x}{\partial \bar{\mathbf{p}}_g}\right|_{12\times9} \\ \left.\frac{\partial \bar{\mathbf{f}}_\mathrm{w}}{\partial \bar{\mathbf{x}}}\right|_{9\times12} & \left.\frac{\partial \bar{\mathbf{f}}_\mathrm{w}}{\partial \bar{\mathbf{p}}_w}\right|_{9\times9} & \left.\frac{\partial \bar{\mathbf{f}}_\mathrm{w}}{\partial \bar{\mathbf{p}}_g}\right|_{9\times9} \\ \left.\frac{\partial \bar{\mathbf{f}}_\mathrm{g}}{\partial \bar{\mathbf{x}}}\right|_{9\times12} & \left.\frac{\partial \bar{\mathbf{f}}_\mathrm{g}}{\partial \bar{\mathbf{p}}_w}\right|_{9\times9} & \left.\frac{\partial \bar{\mathbf{f}}_\mathrm{g}}{\partial \bar{\mathbf{p}}_g}\right|_{9\times9} \end{bmatrix} \tag{B.33}$$

References

Alfano, G., Crisfield, M.A., 2001. Finite element interface models for the delamination analysis of laminated composites: Mechanical and computational issues. Internat. J. Numer. Methods Engrg. 50 (7), 1701–1736. http://dx.doi.org/10.1002/nme.93.

Alonso, E., Olivella, S., Arnedo, D., 2006. Mechanisms of gas transport in clay barriers. Cuad. Geol. Ibér.=J. Iber. Geol.: Int. Publ. Earth Sci. 32 (32), 175–196. http://dx.doi.org/10.5209/JIGE.33931.

Arnedo, D., Alonso, E.E., Olivella, S., 2013. Gas flow in anisotropic claystone: modelling triaxial experiments. Int. J. Numer. Anal. Methods Geomech. 37, 2239–2256. http://dx.doi.org/10.1002/nag.2132.

Arnedo, D., Alonso, E.E., Olivella, S., Romero, E., 2008. Gas injection tests on sand/bentonite mixtures in the laboratory. experimental results and numerical modelling. Phys. Chem. Earth 33, S237–S247. http://dx.doi.org/10.1016/j.pce.2008.10.061.

Arnold, D.N., 1990. Mixed finite element methods for elliptic problems. Comput. Methods Appl. Mech. Engrg. 82, 281–300.

Arnold, P., Vardon, P.J., Hicks, M.A., Fokkens, J., Fokker, P.A., 2015. A Numerical and Reliability Based Investigation into the Feasibility of a Dutch Radioactive Waste Repository in Boom Clay. Technical Report OPERA-PU-TUD311 (COVRA), p. 316, URL https://www.covra.nl/app/uploads/2019/08/OPERA-PU-TUD311.pdf.

Brezzi, F., Bathe, K.-J., 1990. A discourse on the stability conditions for mixed finite element formulations. Comput. Methods Appl. Mech. Engrg. 82, 27–57.

Carol, I., López, C.M., Roa, O., 2001. Micromechanical analysis of quasi brittle materials using fracture based interface elements. Internat. J. Numer. Methods Engrg. 52, 193–215. http://dx.doi.org/10.1002/nme.277.

Carrier, B., Granet, S., 2012. Numerical modeling of hydraulic fracture problem in permeable medium using cohesive zone model. Eng. Fract. Mech. 79, 312–328. http://dx.doi.org/10.1016/j.engfracmech.2011.11.012.

Cerfontaine, B., Dieudonné, A.C., Radu, J.P., Collin, F., Charlier, R., 2015. 3D zero-thickness coupled interface finite element: cccformulation and application. Comput. Geotech. 69, 124–140. http://dx.doi.org/10.1016/j.compgeo.2015.04.016.

Chittenden, N., Benbow, S., Bond, A., Norris, S., 2020. Development of an upscalable HM model for representing advective gas migration through saturated bentonite. Int. J. Rock Mech. Min. Sci. 133 (January), 104415. http://dx.doi.org/10.1016/j.ijrmms.2020.104415.

Collin, F., 2003. Couplages Thermo-Hydro-Mécaniques Dans les Sols et les Roches Tendres Partiellement Saturés (Ph.D. thesis). Université de Liège, p. 300.

Collin, F., Li, X.L., Radu, J.P., Charlier, R., 2002. Thermo-hydro-mechanical coupling in clay barriers. Eng. Geol. 64 (2–3), 179–193. http://dx.doi.org/10.1016/S0013-7952(01)00124-7.

Cuss, R., Harrington, J., Giot, R., Auvray, C., 2014. Experimental observations of mechanical dilation at the onset of gas flow in Callovo-Oxfordian claystone. Geol. Soc. Spec. Publ. 400 (1), 507–519. http://dx.doi.org/10.1144/SP400.26.

Dagher, E.E., Nguyen, T.S., Infante Sedano, J.A., 2019. Development of a mathematical model for gas migration (Two-phase flow) in natural and engineered barriers for radioactive waste disposal. Geol. Soc. Spec. Publ. 482 (1), 115–148. http://dx.doi.org/10.1144/SP482.14.

Damians, I.P., Olivella, S., Gens, A., 2020. Modelling gas flow in clay materials incorporating material heterogeneity and embedded fractures. Int. J. Rock Mech. Min. Sci. 136 (October), 104524. http://dx.doi.org/10.1016/j.ijrmms.2020.104524.

Daniels, K., Harrington, J., 2017. The Response of Compact Bentonite during a 1-D Gas Flow Test. Open Report OR/17/067 Technical Report, British Geological Survey.

Delahaye, C.H., Alonso, E.E., 2002. Soil heterogeneity and preferential paths for gas migration. Eng. Geol. 64 (2–3), 251–271. http://dx.doi.org/10.1016/S0013-7952(01)00104-1.

Dieudonné, A.C., Cerfontaine, B., Collin, F., Charlier, R., 2015. Hydromechanical modelling of shaft sealing for CO2 storage. Eng. Geol. 193, 97–105. http://dx.doi.org/10.1016/j.enggeo.2015.04.016.

van Genuchten, M.T., 1980. A closed-form equation for predicting the hydraulic conductivity of unsaturated soils. Soil Sci. Am. J. 44 (5), 892–898.

Gerard, P., Charlier, R., Chambon, R., Collin, F., 2008. Influence of evaporation and seepage on the convergence of a ventilated cavity. Water Resour. Res. 44 (7), http://dx.doi.org/10.1029/2007WR006500.

Gerard, P., Harrington, J., Charlier, R., Collin, F., 2014. Modelling of localised gas preferential pathways in claystone. Int. J. Rock Mech. Min. Sci. 67, 104–114. http://dx.doi.org/10.1016/j.ijrmms.2014.01.009.

Gonzalez-Blanco, L., Romero, E., Jommi, C., Li, X., Sillen, X., 2016. Gas migration in a cenozoic clay: Experimental results and numerical modelling. Geomech. Energy Environ. 6, 81–100. http://dx.doi.org/10.1016/j.gete.2016.04.002.

Graham, C.C., Harrington, J.F., Sellin, P., 2016. Gas migration in pre-compacted bentonite under elevated pore-water pressure conditions. Appl. Clay Sci. 132–133, 353–365. http://dx.doi.org/10.1016/j.clay.2016.06.029.

Guo, G., Fall, M., 2018. Modelling of dilatancy-controlled gas flow in saturated bentonite with double porosity and double effective stress concepts. Eng. Geol. 243 (January), 253–271. http://dx.doi.org/10.1016/j.enggeo.2018.07.002.

Guo, G., Fall, M., 2019. Modelling of preferential gas flow in heterogeneous and saturated bentonite based on phase field method. Comput. Geotech. 116 (July), 103206. http://dx.doi.org/10.1016/j.compgeo.2019.103206.

Gutiérrez-Rodrigo, V., Martín, P.L., Villar, M.V., 2021. Effect of interfaces on gas breakthrough pressure in compacted bentonite used as engineered barrier for radioactive waste disposal. Process Saf. Environ. Prot. 149, 244–257. http://dx.doi.org/10.1016/j.psep.2020.10.053.

Harrington, J.F., Graham, C.C., Cuss, R.J., Norris, S., 2017. Gas network development in a precompacted bentonite experiment: Evidence of generation and evolution. Appl. Clay Sci. 147 (July), 80–89. http://dx.doi.org/10.1016/j.clay.2017.07.005.

Harrington, J.F., Graham, C.C., Cuss, R.J., Norris, S., 2019. Gas network development in compact Bentonite: Key controls on the stability of flow pathways. Geofluids 2019, http://dx.doi.org/10.1155/2019/3815095.

Harrington, J.F., de la Vaissière, R., Noy, D.J., Cuss, R.J., Talandier, J., 2012. Gas flow in Callovo-Oxfordian claystone (COx): results from laboratory and field-scale measurements. Mineral. Mag. 76 (8), 3303–3318. http://dx.doi.org/10.1180/minmag.2012.076.8.43.

Haynes, W.M. (Ed.), 2014. CRC Handbook of Chemistry and Physics, ninety fifth ed. CRC Press, Boca Raton (FL).

Horseman, S.T., Harrington, J.F., Sellin, P., 1999. Gas migration in clay barriers. Eng. Geol. 54, 139–149.

Idiart, A.E., López, C.M., Carol, I., 2011a. Chemo-mechanical analysis of concrete cracking and degradation due to external sulfate attack: A meso-scale model. Cem. Concr. Compos. 33 (3), 411–423. http://dx.doi.org/10.1016/j.cemconcomp.2010.12.001.

Idiart, A.E., López, C.M., Carol, I., 2011b. Modeling of drying shrinkage of concrete specimens at the meso-level. Mater. Struct. 44 (2), 415–435. http://dx.doi.org/10.1617/s11527-010-9636-2.

Jacops, E., Volckaert, G., Maes, N., Weetjens, E., Govaerts, J., 2013. Determination of gas diffusion coefficients in saturated porous media: He and CH4 diffusion in boom clay. Appl. Clay Sci. 83–84, 217–223. http://dx.doi.org/10.1016/j.clay.2013.08.047.

Lequesne, C., 2009. Modeling of Fracture in Heavy Steel Welded Column Connection Submitted to Cyclic Loading by Finite Elements (Ph.D. thesis). Universitè de Liège.

Levasseur, S., Collin, F., Daniels, K., Dymitrowska, M., Harrington, J., Jacops, E., Kolditz, O., Marschall, P., Norris, S., Sillen, X., Talandier, J., Truche, L., Wendling, J., 2021. Initial state of the art on gas transport in clayey materials. deliverable D6.1 of the HORIZON 2020 project EURAD, work package gas. EC grant agreement no: 847593. URL https://www.ejp-eurad.eu/sites/default/files/2021-11/EURAD%20Deliverable%20D6.1_SOTA1%20%281%29.pdf.

Liaudat, J., Carol, I., López, C.M., 2020. Model for alkali-silica reaction expansions in concrete using zero-thickness chemo-mechanical interface elements. Int. J. Solids Struct. 207, 145–177. http://dx.doi.org/10.1016/j.ijsolstr.2020.09.019.

López, C.M., 1999. Análisis Microestructural de La Fractura del Hormigón Utilizando Elementos Finitos Tipo Junta. aplicación a Diferentes Hormigones (Ph.D. thesis). Universitat Politècnica de Catalunya.

López, C.M., Carol, I., Aguado, A., 2008. Meso-structural study of concrete fracture using interface elements. I: numerical model and tensile behavior. Mater. Struct. 41 (3), 583–599. http://dx.doi.org/10.1617/s11527-007-9314-1.

Marschall, P., Horseman, S., Gimmi, T., 2005. Characterisation of gas transport properties of the opalinus clay, a potential host rock formation for radioactive waste disposal. Oil Gas Sci. Technol. 60 (1), 121–139. http://dx.doi.org/10.2516/ogst:2005008.

Mertens, J., Bastiaens, W., Dehandschutter, B., 2004. Characterisation of induced discontinuities in the boom clay around the underground excavations (URF, Mol, Belgium). Appl. Clay Sci. 26 (1-4 SPEC. ISS.), 413–428. http://dx.doi.org/10.1016/j.clay.2003.12.017.

Mi, Y., Crisfield, M.A., Davies, G., Hellweg, H.-B., 1998. Progressive delamination using interface elements. J. Compos. Mater. 32, 1246–1272.

Miehe, C., Hofacker, M., Welschinger, F., 2010. A phase field model for rate-independent crack propagation: Robust algorithmic implementation based on operator splits. Comput. Methods Appl. Mech. Engrg. 199 (45–48), 2765–2778. http://dx.doi.org/10.1016/j.cma.2010.04.011.

Nguyen, V.P., 2014. An open source program to generate zero-thickness cohesive interface elements. Adv. Eng. Softw. 74, 27–39. http://dx.doi.org/10.1016/j.advengsoft.2014.04.002.

Nguyen, V.P., Lian, H., Rabczuk, T., Bordas, S., 2017. Modelling hydraulic fractures in porous media using flow cohesive interface elements. Eng. Geol. 225 (November 2016), 68–82. http://dx.doi.org/10.1016/j.enggeo.2017.04.010.

Olivella, S., Alonso, E.E., 2008. Gas flow through clay barriers. Geotechnique 58 (3), 157–176. http://dx.doi.org/10.1680/geot.2008.58.3.157.

Ortiz, L., Volckaert, G., Mallants, D., 2002. Gas generation and migration in Boom Clay, a potential host rock formation for nuclear waste storage. Eng. Geol. 64, 287–296. http://dx.doi.org/10.1016/S0013-7952(01)00107-7.

Pandolfi, A., Ortiz, M., 1998. Solid modeling aspects of three-dimensional fragmentation. Eng. Comput. 14 (4), 287–308. http://dx.doi.org/10.1007/BF01201761.

Rueda-Cordero, J.A., Mejia-Sanchez, E.C., Roehl, D., 2019a. Hydromechanical modeling of unrestricted crack propagation in fractured formations using intrinsic cohesive zone model. Eng. Fract. Mech. 221 (August), 106655. http://dx.doi.org/10.1016/j.engfracmech.2019.106655.

Rueda-Cordero, J.A., Mejia-Sanchez, E.C., Roehl, D., Cabral-Pereira, L., 2019b. Hydro-mechanical modeling of hydraulic fracture propagation and its interactions with frictional natural fractures. Comput. Geotech. 111 (March), 290–300. http://dx.doi.org/10.1016/j.compgeo.2019.03.020.

Sander, R., 2015. Compilation of Henry's law constants (version 4.0) for water as solvent. Atmos. Chem. Phys. 15, 4399–4981. http://dx.doi.org/10.5194/acp-15-4399-2015.

Segura, J.M., Carol, I., 2004. On zero-thickness interface elements for diffusion problems. Int. J. Numer. Anal. Methods Geomech. 28 (9), 947–962. http://dx.doi.org/10.1002/nag.358.

Segura, J.M., Carol, I., 2008a. Coupled HM analysis using zero-thickness interface elements with double nodes - Part II: Verification and application. Int. J. Numer. Anal. Methods Geomech. 32, 2103–2123. http://dx.doi.org/10.1002/nag.730CoupledHManalysis.

Segura, J.M., Carol, I., 2008b. Coupled HM analysis using zero-thickness interface elements with double nodes. Part I: Theoretical model. Int. J. Numer. Anal. Methods Geomech. 32, 2083–2101. http://dx.doi.org/10.1002/nag.735.

Senger, R., Lanyon, B., Marschall, P., Vomvoris, S., Fujiwara, A., 2008. Numerical modeling of the gas migration test at the grimsel test site (Switzerland). Nucl. Technol. 164 (2), 155–168. http://dx.doi.org/10.13182/NT08-A4016.

Senger, R., Romero, E., Marschall, P., 2018. Modeling of gas migration through low-permeability clay rock using information on pressure and deformation from fast air injection tests. Transp. Porous Media 123 (3), 563–579. http://dx.doi.org/10.1007/s11242-017-0962-5.

Tang, C.S., Pei, X.J., Wang, D.Y., Shi, B., Li, J., 2015. Tensile strength of compacted clayey soil. J. Geotech. Geoenviron. Eng. 141 (4), 1–8. http://dx.doi.org/10.1061/(ASCE)GT.1943-5606.0001267.

Trabelsi, H., Romero, E., Jamei, M., 2018. Tensile strength during drying of remoulded and compacted clay: The role of fabric and water retention. Appl. Clay Sci. 162 (May), 57–68. http://dx.doi.org/10.1016/j.clay.2018.05.032.

Vargaftik, N.B., Volkov, B.N., Voljak, L.D., 1983. International tables of the surface tension of water. http://dx.doi.org/10.1063/1.555688.

Volckaert, G., Bernier, F., Sillen, X., Van Geet, M., Mayor, J., Göbel, I., Blümling, P., Frieg, B., Su, K., 2004. Similarities and differences in the behaviour of plastic and indurated clays. In: 6th European Commission Conference on the Management and Disposal of Radioactive Waste (Euradwaste'04), Community Policy and Research & Training Activities. pp. 281–291.

Volckaert, G., Ortiz, L., de Cannière, P., 1995. MEGAS: Modelling and experiments on gas migration in repository host rocks. Technical Report, European Commission, Directorate-General for Research and Innovation, Luxenbourg, p. 464, URL https://op.europa.eu/en/publication-detail/-/publication/0eacb006-b0e5-435a-877b-551a6fd658ea.

Wang, J.J., Zhu, J.G., Chiu, C.F., Zhang, H., 2007. Experimental study on fracture toughness and tensile strength of a clay. Eng. Geol. 94 (1–2), 65–75. http://dx.doi.org/10.1016/j.enggeo.2007.06.005.

Xu, W.J., Shao, H., Hesser, J., Wang, W., Schuster, K., Kolditz, O., 2013. Coupled multiphase flow and elasto-plastic modelling of in-situ gas injection experiments in saturated claystone (Mont Terri Rock Laboratory). Eng. Geol. 157, 55–68. http://dx.doi.org/10.1016/j.enggeo.2013.02.005.

Yang, J., Fall, M., 2021a. A dual porosity poroelastic model for simulation of gas flow in saturated claystone as a potential host rock for deep geological repositories. Tunn. Undergr. Space Technol. 115, 104049. http://dx.doi.org/10.1007/s00603-020-02152-w.

Yang, J., Fall, M., 2021b. Coupled hydro-mechanical modelling of di- latancy controlled gas flow and gas induced fracturing in saturated claystone. Int. J. Rock Mech. Min. Sci. 138, 104584. http://dx.doi.org/10.1016/j.ijrmms.2020.104584.

Yang, J., Fall, M., Guo, G., 2020. A three-dimensional hydro-mechanical model for simulation of dilatancy controlled gas flow in anisotropic claystone. Rock Mech. Rock Eng. 53, 4091–4116. http://dx.doi.org/10.1007/s00603-020-02152-w.